



CornerSense: Virtual Path-augmented WiFi Sensing for Human Proximity Detection Around Corners on Mobile Robots

JING HE, The Chinese University of Hong Kong, Hong Kong, China

RUI ZHANG, Shenzhen University, Guangdong, China

QIJIA WANG, The Chinese University of Hong Kong, Hong Kong, China

RUIQI KONG, The Chinese University of Hong Kong, Hong Kong, China

HE CHEN*, The Chinese University of Hong Kong, Hong Kong, China

WiFi sensing has attracted significant attention over the past decade for its potential to enable ubiquitous human activity monitoring. While prior approaches primarily rely on stationary transceivers, this paper is the first to investigate the feasibility of WiFi sensing on mobile robots. We introduce CornerSense, a new framework that empowers mobile robots to leverage their WiFi interfaces for detecting human proximity around corners, effectively addressing the non-line-of-sight challenges commonly encountered by traditional robotic sensors such as cameras and LiDAR. Our analysis demonstrates that the design of CornerSense fundamentally differs from, and is more challenging than, conventional WiFi sensing with stationary transceivers. In particular, the intertwined movement of the robot and nearby humans complicates the isolation of human-induced signal variations, which is critical for accurate proximity detection. To address this challenge, CornerSense develops a virtual path-augmented, two-stage dominant path extraction approach based on principal component analysis (PCA). In the first stage, through strategically introducing a virtual path, CornerSense extracts a reference path that incorporates only the robot's motion by applying PCA on the power of the virtual path-augmented channel state information (aug-CSI). During the second stage, the reference path is first subtracted from the aug-CSI. This subtraction allows for a second application of PCA to the power of the residual aug-CSI, thereby enabling the extraction of another distinct dominant path that is reflected off the human body before arriving at the robot. This path is referred to as the dominant human-reflected path. Finally, the reference path extracted in the first stage is employed to compensate for the hardware-induced phase offset in the dominant human-reflected path, yielding cleaned CSI ready for accurate and robust detection of human proximity. Real-world experimental evaluations conducted across nine different corners in three groups and under four distinct human walking patterns reveal that CornerSense achieves an average true positive rate (TPR) of 96% while maintaining a low average false positive rate (FPR) of 3%. In contrast, a baseline system that directly applies an algorithm intended for stationary transceiver-based proximity sensing only reaches a TPR of 84% and suffers from a markedly higher FPR of 46%, which is over an order of magnitude higher than that of CornerSense.

CCS Concepts: • **Human-centered computing** → Ubiquitous and mobile computing systems and tools.

Additional Key Words and Phrases: Mobile WiFi sensing, mobile robot, human proximity detection around corners, principal component analysis.

*He Chen is the corresponding author.

Authors' Contact Information: Jing He, The Chinese University of Hong Kong, Hong Kong, China, 1155195749@link.cuhk.edu.hk; Rui Zhang, Shenzhen University, Guangdong, China, zhrrygh@szu.edu.cn; Qijia Wang, The Chinese University of Hong Kong, Hong Kong, China, wq025@ie.cuhk.edu.hk; Ruiqi Kong, The Chinese University of Hong Kong, Hong Kong, China, ruiqikong@cuhk.edu.hk; He Chen, The Chinese University of Hong Kong, Hong Kong, China, he.chen@ie.cuhk.edu.hk.



This work is licensed under a Creative Commons Attribution-NonCommercial 4.0 International License.

© 2025 Copyright held by the owner/author(s).

ACM 2474-9567/2025/12-ART181

<https://doi.org/10.1145/3770699>

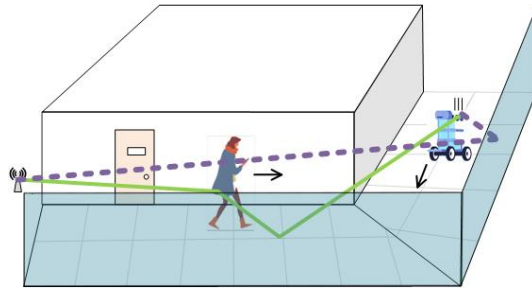


Fig. 1. Scenario of WiFi-based passive human proximity sensing at corners for mobile robots.

ACM Reference Format:

Jing He, Rui Zhang, Qijia Wang, Ruiqi Kong, and He Chen. 2025. CornerSense: Virtual Path-augmented WiFi Sensing for Human Proximity Detection Around Corners on Mobile Robots. *Proc. ACM Interact. Mob. Wearable Ubiquitous Technol.* 9, 4, Article 181 (December 2025), 37 pages. <https://doi.org/10.1145/3770699>

1 INTRODUCTION

WiFi has expanded its role from a mere conduit for communication to a multi-dimensional wireless sensing technology in recent decades, driven by its ubiquitous deployment and cost efficiency. WiFi sensing, when compared to traditional sensors such as camera, radar, and ultrasound, compensates for the perceptive capabilities of devices integrated into WiFi networks, especially in conditions of low visibility, non-line-of-sight (NLoS) scenarios, and noisy environments [3, 46, 58]. WiFi sensing has enabled a vast array of passive sensing applications including presence detection [18, 29, 57], gait recognition [41, 55, 56], and activity recognition [42, 43, 49]. Despite significant advancements, the prevailing passive WiFi sensing algorithms are mostly limited to scenarios where the transceivers are stationary. This constraint narrows the scope of WiFi sensing for mobile robots, which play an increasingly critical role in various applications, from industrial to domestic [15, 24, 31]. These robots are pivotal in improving the synergy between mechanical systems, spatial environments, and human interactions [20, 28, 37], and they must continuously sense their surroundings to enhance human safety, even while in motion. Given the increasing prevalence of mobile robots getting connected via WiFi, it is both intriguing and valuable to investigate the potential of WiFi sensing capabilities on these dynamic platforms.

This paper conducts the first exploration of passive WiFi sensing on mobile robots. Our research specifically targets the practical and critical challenge of passively detecting human proximity at corners, a key capability for mobile robots to prevent potential collisions with approaching humans. In the considered scenario where corners create NLoS challenges, WiFi sensing presents a compelling solution, as it can address the limitations typically faced by widely-used robot sensors such as cameras and LiDARs. To assess the impact of a mobile WiFi receiver's (Rx) movement on WiFi sensing capabilities, we conducted preliminary experiments employing a cutting-edge WiFi-based proximity detection algorithm as a benchmark. The results reveal that the algorithm frequently issues alerts when the Rx, mounted on a mobile robot, approaches corners, irrespective of the presence of a person behind corners. This suggests that existing WiFi sensing methods, designed for stationary transceivers, fall short of addressing the sensing needs of mobile robots.

The core challenge arises from the fact that previous WiFi sensing setups involve stationary transceivers, wherein signal propagation paths are largely stable, with changes occurring only due to the movement of to-be-sensed targets [11, 12, 14, 40, 42, 44, 45, 47, 48]. These variations in the received signal are distinct indicators of the targets' motion, which existing WiFi sensing technologies are designed to detect. In contrast, when a moving robot conducts the sensing task, its own motion introduces changes to all signal paths, influenced by the angles between the robot's trajectory and the signal paths. This results in the targets' motion being masked by that of

the robot, further complicated by multipath effects, thus disrupting the basic principles upon which previous WiFi sensing methods are built. Consequently, WiFi sensing algorithms designed for stationary transceivers face significant difficulties in adapting to scenarios with mobile Rx(s).

Although WiFi-based sensing on mobile robots remains an open research challenge, several prior efforts have investigated wireless sensing on mobile platforms using alternative modalities. Notably, recent studies have developed mobile sensing systems based on wideband radar technologies [10, 51, 52]. By exploiting the fine-grained spatial resolution enabled by the large bandwidth of radar devices, these approaches are able to directly separate two critical signal components from the received radar signal: the reference path, originating from a stationary object and influenced solely by the robot's motion, and the human-reflected path, which involves the combined motion of both the robot and the human target. The influence of the robot's movement can subsequently be removed by normalizing the human-reflected signal¹ with respect to the reference path. However, the methods proposed in [10, 51, 52] may not be directly applicable to WiFi sensing, as the limited bandwidth of WiFi systems constrains the spatial resolution required to accurately distinguish between the reference path and the human-reflected path within the channel state information (CSI) extracted from received WiFi signals. A similar conclusion has also been articulated in the discussion section of [52]. Furthermore, in comparison to radar systems, WiFi-based systems are subject to additional signal distortions arising from the bistatic configuration of WiFi transceivers, such as carrier frequency offsets and sampling frequency offsets. These hardware-induced distortions can easily obscure the subtle signal variations caused by human motion, significantly degrading the accuracy of proximity detection. These challenges, which are unique to WiFi sensing systems, necessitate the development of a novel and effective framework that can extract critical signal components and compensate for the effects of both robot motion and hardware-induced distortions, thereby enabling accurate and robust WiFi-based human proximity detection around corners for mobile robots.

To tackle the aforementioned challenges, this paper introduces CornerSense, the first virtual path-augmented WiFi sensing framework designed to enable mobile robots to reliably sense human proximity around corners while in motion. CornerSense is designed with privacy preservation in mind, focusing solely on detecting human proximity without collecting or inferring any personal characteristics such as body shape and habitual postures. At the core of CornerSense are carefully designed methods for reference path extraction, dominant human-reflected path extraction, and robot motion and hardware distortion compensation, which together enable robust passive WiFi sensing on moving robots. Our main contributions are as follows:

- We develop an efficient reference path extraction method that identifies a reference path capturing only the robot's motion and hardware-induced phase offset. This is achieved by strategically introducing a virtual path into raw CSI measurements collected by the mobile robot. The virtual path-augmented CSI is termed aug-CSI. We further refer to the power of the aug-CSI as the aug-CSI power. The virtual path ensures that the signal components corresponding to the reference path dominate the aug-CSI power, facilitating their extraction through principal component analysis (PCA).
- We devise and implement an effective robot motion and phase offset compensation (RMPOC) algorithm that compensates both the robot's motion and the phase offset from the dominant human-reflected path. The algorithm first removes the reference path from the aug-CSI to obtain residual aug-CSI, where the dominant human-reflected path stands out as the primary component, enabling its extraction through another application of PCA. Then, by leveraging the extracted reference path and the known robot's velocities, the robot's motion and the phase offset in the dominant human-reflected path can be effectively

¹Since the human body dimensions are significantly larger than the wavelength of 5.32 GHz WiFi signals (approximately 5.64 cm), the dominant interaction between the signal and the human body is reflection. Accordingly, we consistently use the term "reflected" throughout this paper to describe this interaction.

compensated. This results in cleaned CSI data that exclusively captures human-induced signal variations, thereby enabling accurate and reliable human proximity detection.

- We propose a new subcarrier phase difference metric that intuitively captures path length variations induced by human motion, enabling effective detections of human proximity using cleaned CSI data. We then systematically evaluate the human proximity detection performance of CornerSense across nine different corners in three groups and under four different walking patterns. Our experimental results demonstrate that CornerSense achieves a consistent 96% true positive rate (TPR) for proximity detection, coupled with an $15.3\times$ reduced false positive rate (FPR) compared to a baseline proximity detection method originally designed for stationary transceivers.

The code and the CSI data used in this paper will be made available at: <https://github.com/hj5202/CornerSense.git>.

2 BACKGROUND AND MOTIVATION

In this section, we begin by providing a concise overview of the CSI models for scenarios involving stationary and mobile Rx, respectively. We then delve into the challenges of human proximity detection that arise when the receiver on mobile robots is in motion.

2.1 CSI Model for a Stationary Rx

WiFi systems employ orthogonal frequency division multiplexing (OFDM) techniques for data transmission. The CSI, estimated for data recovery on the Rx side, captures the channel's frequency response over multiple orthogonal subcarriers. The CSI provides detailed insights into the signal variations from the transmitter (Tx) to the Rx across each subchannel [32]. Passive motion sensing of moving targets, using the CSI received at Rx, typically involves decomposing the composite CSI representation into two categories: static paths, encompassing the line-of-sight (LoS) path if exists and paths reflecting off stationary objects; and dynamic paths, which are associated with reflections off moving objects. Consequently, the CSI for a subcarrier at frequency f and time t_n can be expressed as

$$H(f, t_n) = e^{-j\vartheta(f, t_n)} \left\{ H_s(f) + \sum_{i \in \Omega(t_n)} A_i(f, t_n) e^{-j\frac{2\pi f}{c} l_i(t_n) - j\sigma_i(t_n)} \right\}, \quad (1)$$

where $t_n = t_{n-1} + \Delta t$, $n = 1, \dots, N$, $H_s(f)$ represents the static component associated with static paths, and $\Omega(t_n)$ denotes the set of dynamic paths affected by the moving target at time t_n . In (1), $A_i(f, t_n)$ and $l_i(t_n)$ represent the channel coefficient magnitude and the length of the i -th path at time t_n , respectively, c stands for the speed of light, and $\sigma_i(t_n)$ represents the phase variations caused by reflection and scattering. $\vartheta(f, t_n)$ denotes the phase offset caused by hardware impairments associated with WiFi transceivers² [34]. While the static component $H_s(f)$ remains constant over time, the dynamic component is time-variant due to changes in the path length $l_i(t_n)$.

To characterize the mathematical relationship between path length variation and target motion, we present a scenario in Figure 2(a) where an individual is approaching a corner at speed $v_p(t_n)$. For the sake of clarity, we depict one propagation path from the Tx, an access point (AP), to the Rx to represent the dynamic path. The path reaches the Rx with the angle of arrival (AoA) $\theta_i(t_n)$ at time t_n . We define the path length change rate (PLCR) of the i -th path within $\Omega(t_n)$, influenced by the target's motion, as $v_i(t_n) = v_p(t_n) - v_p(t_n) \sin(\theta_i(t_n))$. This expression indicates that the individual moves roughly in a straight along the corridor, thereby neglecting the negligible angle between the person's direction of movement and the line connecting the target and the AP [17, 38]. Consequently, the length of the i -th path at time t_n is given by $l_i(t_n) = l_i(t_{n-1}) + v_i(t_n) \Delta t$. Here, Δt is sufficiently small, allowing us to treat $v_i(t_n)$ as a constant within this short interval.

²The hardware-induced magnitude distortions are assumed to be absorbed into the magnitudes of the channel coefficients.

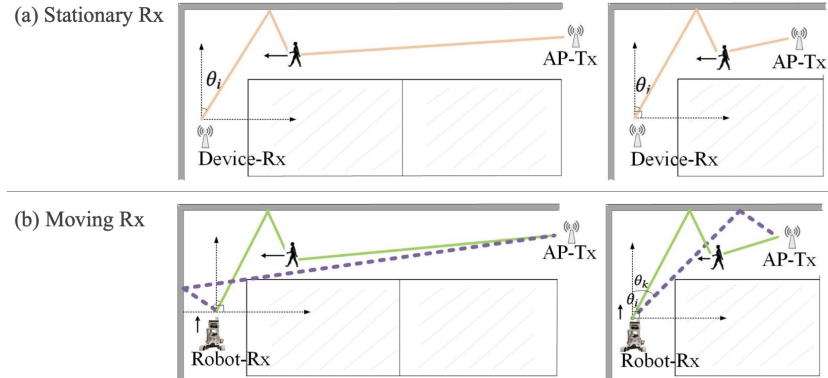


Fig. 2. Comparison of WiFi-based human proximity sensing with stationary and moving receivers across different AP locations: AP far from the corner (Left) and AP close to the corner (Right). Note that when the Rx on the robot is moving, a reference path (indicated by the purple dashed line) that captures only the robot’s speed (i.e., $v_m(t_n)$) always exists. The reference path pattern differs in the corner scenario due to human blockage when AP is close to the target, see the right of subfigure (b).

2.2 CSI Model for a Moving Rx

When the Rx is on a mobile robot moving toward the corner, the path lengths for both static and dynamic paths in Equation 1 exhibit temporal variations. This introduces two distinct categories of dynamic paths, exemplified in Figure 2(b): the set of purple dashed paths $\Omega_1(t_n)$ and the set of green solid paths $\Omega_2(t_n)$. Consequently, the CSI $H(f, t_n)$ can be expressed as

$$H(f, t_n) = e^{-j\vartheta(f, t_n)} \left\{ \sum_{k \in \Omega_1(t_n)} A_k(f, t_n) e^{-j\frac{2\pi f}{c} l_k(t_n) - j\sigma_k(t_n)} + \sum_{i \in \Omega_2(t_n)} A_i(f, t_n) e^{-j\frac{2\pi f}{c} l_i(t_n) - j\sigma_i(t_n)} \right\}, \quad (2)$$

where $A_k(\cdot, \cdot)$ represents the magnitude of the channel coefficient of the k -th path in $\Omega_1(t_n)$ and $A_i(\cdot, \cdot)$ represents that of the i -th path in $\Omega_2(t_n)$. $\sigma_k(t_n)$ and $\sigma_i(t_n)$ are the reflection and scattering induced phase changes of the k -th path in $\Omega_1(t_n)$ and the i -th path in $\Omega_2(t_n)$, respectively. $l_k(t_n) = l_k(t_{n-1}) + v_k(t_n)\Delta t$ is the length of paths in $\Omega_1(t_n)$, where $v_k(t_n)$ represents the PLCR of $l_k(t_n)$. Similarly, $l_i(t_n) = l_i(t_{n-1}) + v_i(t_n)\Delta t$ is the length of paths in $\Omega_2(t_n)$, where $v_i(t_n)$ is the change rate of $l_i(t_n)$ in $\Omega_2(t_n)$.

We proceed to analyze the two distinct categories of dynamic paths in further detail. *The first type of dynamic paths*, represented by the purple dashed path in Figure 2(b). These paths initially involved only reflections from stationary objects and are now designated as $\Omega_1(t_n)$. As shown by the purple dashed line in Figure 2(b), these paths only involve the robot’s movement without human interaction. The PLCR of these paths can be obtained by projecting the robot’s velocity onto the direction of the path. Specifically, when the robot moves with velocity $v_m(t_n)$, its projection on the path direction determines the rate at which the path length changes. This projection can be calculated using the cosine of the angle between the robot’s movement direction and the path direction. Denote by $\theta_k(t_n)$ the angle of arrival (AoA) at the Rx at time t_n . The PLCR for these paths is then given by $v_k(t_n) = -v_m(t_n) \cos(\theta_k(t_n))$. *The second category of paths* involves the green solid path that reflects off the moving target in Figure 2(b), as analyzed similarly in the preceding subsection. The PLCR for this human-reflected path needs to consider both the human and robot movements. As illustrated by the green solid line in Figure 2(b), when a person moves with velocity $v_p(t_n)$, their movement affects the path length in two segments. First, along the segment from Tx to the person, the person’s movement contributes approximately $v_p(t_n)$ to the path length change. Second, along the segment from the person to the robot, the projection of the person’s velocity contributes approximately $-v_p(t_n) \sin(\theta_i(t_n))$, where $\theta_i(t_n)$ denotes the angle between the green path and the

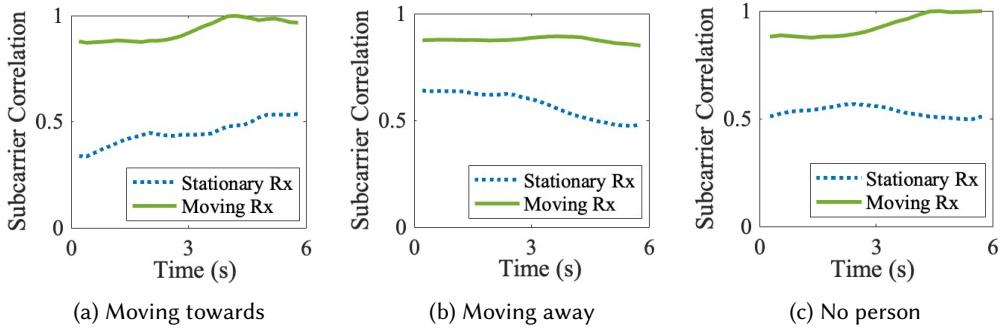


Fig. 3. Comparison of the subcarrier correlation metric [21] across three distinct human motion cases, illustrating the differences between stationary and moving Rx.

robot's trajectory. Additionally, we also need to account for the robot's movement effect on this path, which contributes $-v_m(t_n) \cos(\theta_i(t_n))$ through its velocity projection onto the path. Therefore, the PLCR for this path is formulated as $v_i(t_n) = v_p(t_n) - v_p(t_n) \sin(\theta_i(t_n)) - v_m(t_n) \cos(\theta_i(t_n))$. The expression for v_i clearly illustrates the interplay between human and robot motion. Notably, when the robot's speed $v_m(t_n) = 0$, the PLCR $v_i(t_n)$ is solely attributed to the velocity induced by human movement, aligning with the previously defined $v_i(t_n)$ for a stationary Rx.

2.3 Motivation and Challenges of CornerSense

In the preceding subsections, we have analyzed and distinguished the path dynamics of WiFi sensing with stationary and mobile Rx(s). Building on this foundation, we embark on a preliminary experiment to assess the impact of robot motion on proximity detection around corners. For this purpose, we apply the existing proximity detection algorithm, originally designed for stationary transceivers, to analyze the CSI data collected by stationary and mobile Rx. To the best of our knowledge, the algorithm presented in [21] is the latest WiFi-based solution for detecting proximity with stationary transceivers. The work [21] introduces a novel metric known as subcarrier correlation, which serves as an indicator of human proximity: an increase in subcarrier correlation suggests an individual is drawing nearer to the stationary Rx, while a decrease implies the opposite. Within our application, we include an additional scenario where there is no person present beyond the corner. We can promptly infer that, in this case, the subcarrier correlation remains stable.

Figure 3 presents the changes in subcarrier correlation from a representative experiment. As depicted, with a stationary Rx, the subcarrier correlation reliably indicates the presence of a human approaching or departing from the corner, as well as the absence of a person beyond the corner. In contrast, when the CSI data is collected by a moving Rx, such as a mobile robot, the subcarrier correlation tends to rise or exhibit unclear variations as the robot approaches the corner, regardless of whether a human is moving toward or away from the corner, or not present at all. This pattern can consequently result in inaccurate detections of human proximity. The experimental findings outlined in Section 4 validate this conjecture. Specifically, when the algorithm from [21] is directly employed for proximity detection on mobile robots, it results in a high FPR of 46%. In such cases, data indicative of a person moving away from the corner or scenarios where no person is present are mistakenly classified as the person approaching. These results highlight the need for a tailored solution to address the challenges posed by the robot motion in WiFi-based human proximity detection.

Recent studies have investigated similar on-robot mobile sensing problems using wideband radar technologies, such as Mobi²Sense [52] and MSense [10]. These novel frameworks share a common approach: they use a

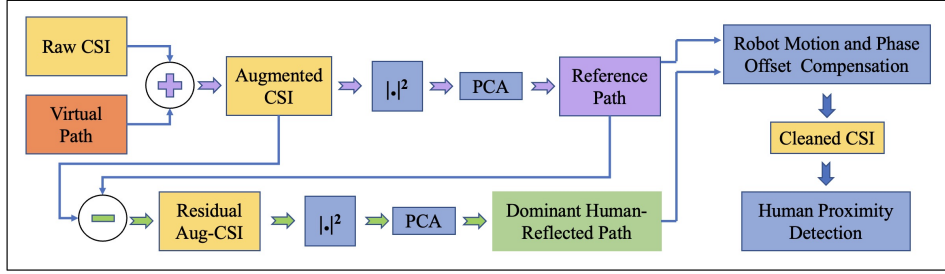


Fig. 4. CornerSense Overview.

reference path reflected by a stationary object to remove the receiver's movement from the signal path reflected by the target, enabling accurate sensing of the target's motion. The separation of these two paths from the received signals is enabled by the fine-grained spatial resolution capability of radar sensors. However, these methods may not be directly applicable to narrowband WiFi sensing due to the limited bandwidth of WiFi signals. The narrow bandwidth restricts the spatial resolution necessary to accurately separate the reference path and the signal path reflected by the target from the CSI of WiFi systems. This limitation hinders the direct application of the aforementioned radar-based techniques to WiFi sensing on mobile robots. The discussion section of [52] also highlights this challenge. The challenge is further exacerbated by the phase offsets inherent in WiFi systems. These phase offsets, caused by clock asynchronism between WiFi transceivers, are not present in radar systems, making it even more difficult to directly adopt radar-based methods for WiFi sensing on mobile platforms. To address these challenges, we introduce CornerSense, a new WiFi sensing framework for mobile robots designed to overcome the limitations of existing methods and enable reliable human proximity detection in real-world scenarios. The following section will provide a detailed description of the CornerSense system and its key components.

3 CORNERSENSE DESIGN

In this section, we first introduce the core idea behind CornerSense, explaining the fundamental principles and objectives that guide its design. Following this, we dive into the design details of each core module that makes up CornerSense. The key signal processing steps of CornerSense is summarized in Figure 4.

3.1 CornerSense Core Idea

Due to the limited bandwidth of WiFi systems, accurately separating a reference path and the dominant path reflected by a human target from CSI measurements is extremely challenging, if not impossible. This limitation drives us to explore an alternative idea: *Given that direct multipath decomposition of CSI measurements is technically challenging, could we instead extract a reference path by applying an effective signal component analysis method to the CSI data?* Our pursuit of this approach is motivated by the observation that, in the considered corner scenarios with NLoS signal propagation, the signal path from the AP to the moving robot via one-off reflection by the wall is typically stronger than those paths that involve multiple reflections by the wall or those that are reflected by the human body before reaching the wall and then the robot, as depicted in Figure 2(b). This is because each additional reflection or interaction with objects in the environment, such as the human body, can lead to increased signal attenuation and thus weaker received signal strength.

The above observation implies that the strongest path among all paths reflected by the wall (i.e., the set $\Omega_1(t_n)$ in Equation 2) should also be the strongest path among all signal paths in the CSI. Consequently, this path becomes an ideal candidate for the reference path for two main reasons. First, the path only contains the

robot's motion and hardware-induced phase offset, as the signal propagates from the AP to the robot via a single reflection off the wall, without any interference from the motion of human target. Second, the stronger signal strength of this path facilitates its extraction from the CSI measurements, making it possible to estimate the phase offset for compensating the hardware-induced distortions, a critical step for achieving for accurate and robust human proximity detection. The entire design of CornerSense is guided by this path extraction idea. As we will demonstrate in Section 3.2, it is indeed possible to solely extract a reference path by analyzing the signal path components of CSI measurements. Moreover, once we can obtain such a reference path, it becomes feasible to extract the dominant human-reflected path. However, the whole process is far from trivial due to the entangled motion effects of the robot and human target within the CSI expression, which are further masked by hardware-induced phase offsets. To address this challenge, we define the aug-CSI power by strategically introducing a virtual path into the CSI measurements. This enables us to extract the signal components of a reference path that solely captures the robot's motion and the phase offset by applying PCA, which are then used to construct the reference path.

With the reference path successfully extracted, our next objective is to isolate a dominant signal path reflected by the human body. Achieving this requires careful analysis to ensure two critical conditions are satisfied. First, we must verify the existence of a strong human-reflected signal path that dominates among all human-related paths. Therefore, it is necessary to remove the initially strongest reference path from the raw CSI. Second, this dominant human-reflected path must be linearly independent of the paths containing only robot motion, thereby enabling its separation. We carefully validate these conditions and subsequently propose an effective robot motion and phase offset compensation (RMPOC) algorithm. The algorithm first removes the impact of robot motion from the two extracted paths, and then leverages the processed reference path to compensate for the phase offset in the dominant human-reflected path. We finally use the resulting cleaned CSI data to perform human proximity detection as if the robot were stationary.

In the following subsections, we will delve into the detailed designs of each core module of CornerSense.

3.2 Motivation and Definition of Aug-CSI Power

Hereafter, we use the subscript r to denote the reference path, which represents the strongest path among all the paths in $\Omega_1(t_n)$. Following the path components defined in Equation 2, the reference path CSI $H_r(f, t_n)$ can be expressed as

$$H_r(f, t_n) \triangleq e^{-j\vartheta(f, t_n)} A_r(f, t_n) e^{-j\frac{2\pi f}{c} l_r(t_n) - j\sigma_r(t_n)}. \quad (3)$$

Recalling the path marked in solid green in Figure 2(b), we have the path length $l_r(t_n) = v_r(t_n)\Delta t + l_r(t_{n-1})$, where $v_r(t_n) = -v_m(t_n) \cos(\theta_r(t_n))$. As discussed in Section 2.2, the robot's movement is captured in the PLCR of $l_r(t_n)$, which appears in the phase of $H_r(f, t_n)$, defined as $-(\frac{2\pi f}{c} l_r(t_n) + \sigma_r(t_n) + \vartheta(f, t_n))$. For mathematical convenience in analyzing PLCR-related expressions, we define $\phi_r(f, t_n) \triangleq \frac{2\pi f}{c} l_r(t_n) + \sigma_r(t_n) + \vartheta(f, t_n)$ and focus on this quantity in the subsequent analysis. To avoid dealing with the exponential terms in the CSI expressions, the power of CSI is often used in phase analysis [42]. In this work, we will apply PCA to perform component analysis for CSI. By applying PCA to the power of CSI measurements, we can effectively analyze the phase information. To proceed, we now provide a brief primer on PCA to familiarize readers with the basic concepts and principles behind this technique.

3.2.1 Direct Application of PCA Does Not Work. We note that previous studies in WiFi sensing with stationary transceivers have applied PCA to isolate human motion from CSI measurements, capturing components that are reflective of the target's movements [42, 48]. In this context, the traditional CSI power formulation can be given

by

$$|H(f, t_n)|^2 = \underbrace{|H_s|^2}_{\textcircled{1}} + \underbrace{\sum_{i \in \Omega(t_n)} A_i^2(f, t_n)}_{\textcircled{2}} + \underbrace{\sum_{i, i' \in \Omega(t_n), i \neq i'} F(f, t_n, i, i')}_{\textcircled{3}} \\ + \underbrace{\sum_{i \in \Omega(t_n)} 2 |H_s| A_i(f, t_n) \cos \left(\frac{2\pi f}{c} l_i(t_n) + \sigma_i(t_n) + \angle H_s \right)}_{\textcircled{4}}, \quad (4)$$

where $\angle H_s$ refers to the phase of H_s and the term

$$F(f, t_n, i, i') = 2A_i(f, t_n)A_{i'}(f, t_n) \cos \left(\frac{2\pi f(l_i(t_n) - l_{i'}(t_n))}{c} + \sigma_i(t_n) - \sigma_{i'}(t_n) \right). \quad (5)$$

In Equation 4, the term $\textcircled{1}$ remains constant over time and the term $\textcircled{2}$ barely changes. The variation of these two components is much smaller than the term $\textcircled{3}$ and term $\textcircled{4}$, which represent the characteristics of the target's movement and may emerge as the principal component in PCA analysis. Given that both Tx and Rx remain stationary, the target movement represents the sole motion within this scenario. The relative contribution of terms $\textcircled{3}$ and $\textcircled{4}$ to the total variance depends on the specific environment configuration. In scenarios with fewer static paths, term $\textcircled{3}$ may dominate the variance due to the direct impact of target motion on the human-selected path. Conversely, in environments with rich static paths, term $\textcircled{4}$ might contribute more significantly to the variance due to the multiple interactions between target motion and static paths. While we cannot definitively determine which terms will emerge as the primary components in PCA, this uncertainty does not affect the phase analysis as any quantities extracted through PCA can effectively serve as indicators to measure the target motion characteristics. This is because they invariably capture the collective impact of target movement on the overall signal propagation.

Unfortunately, in the scenario under consideration, where both the robot and the target are moving simultaneously, applying direct PCA to the CSI power becomes ineffective. To clarify this, we first define the CSI power based on Equation 2 as follows:

$$|H(f, t_n)|^2 = \underbrace{\sum_{k \in \Omega_1(t_n)} A_k^2(f, t_n)}_{\textcircled{1}} + \underbrace{\sum_{i \in \Omega_2(t_n)} A_i^2(f, t_n)}_{\textcircled{2}} + \underbrace{\sum_{k, k' \in \Omega_1(t_n), k \neq k'} F(f, t_n, k, k')}_{\textcircled{3}} \\ + \underbrace{\sum_{k \in \Omega_1(t_n), i \in \Omega_2(t_n)} F(f, t_n, k, i)}_{\textcircled{4}} + \underbrace{\sum_{i, i' \in \Omega_2(t_n), i \neq i'} F(f, t_n, i, i')}. \quad (6)$$

In Equation 6, while the term $\textcircled{1}$ barely changes, the cosine terms in $\textcircled{2}$, $\textcircled{3}$, and $\textcircled{4}$ contain phase information that includes two continuously changing path lengths: one due to the robot motion and another due to the human motion. In this case, it becomes impossible to extract pure human motion components through direct application of PCA, since the path length variations caused by human and robot movements are intrinsically tangled together within these phase terms.

In essence, with the Rx mounted on a mobile robot, all signal paths become dynamic, inherently incorporating the robot's motion, with some paths additionally influenced by potential human motion. In the CSI power expression, all major components arise from interactions between dynamic paths, making it impossible for PCA to isolate "pure" components associated with individual motion effects – components that could otherwise be

readily extracted in simpler scenarios. This fundamental difference necessitates a thorough reconsideration of path component extraction in mobile robot scenarios, thereby motivating our introduction of the power of the virtual path-augmented CSI (aug-CSI power), as elaborated in the next subsection.

3.2.2 Virtual Path and Aug-CSI Power. **Virtual Path:** Through careful observation, we observe that the situation changes significantly when we deliberately introduce a virtual (static) path, with its channel coefficient denoted by H_a . This virtual path is a mathematical construct that does not require any physical hardware modifications or additional reflectors. The amplitude and phase selections of H_a are crucial to our method, where we will demonstrate in the later mathematical derivation (Section 3.3.2) that the amplitude should be $1 \sim 10$ times stronger than the strongest path in raw CSI, and the phase should be set to $\pi/4$ for effective signal decomposition. Furthermore, this intentional path incorporation would yield new terms in the new CSI power, termed aug-CSI power, in which the amplitude and phase of $H_r(f, t_n)$ interact solely with the static path H_a . By applying PCA to the aug-CSI power, we can obtain the cosine component that exclusively represents the phase information of the reference path, without the influence of other dynamic paths.

Aug-CSI Power: To obtain the aug-CSI power, a virtual path H_a is added to achieve the mutual interaction with each dynamic path in Equation 2. Mathematically, aug-CSI is defined as,

$$H_{vi}(f, t_n) \triangleq e^{-j\vartheta(f, t_n)} \left\{ \sum_{k \in \Omega_1(t_n)} A_k(f, t_n) e^{-j\frac{2\pi f}{c}l_k(t_n) - j\sigma_k(t_n)} + \sum_{i \in \Omega_2(t_n)} A_i(f, t_n) e^{-j\frac{2\pi f}{c}l_i(t_n) - j\sigma_i(t_n)} \right\} + H_a. \quad (7)$$

It is worth noting that the virtual path H_a introduced in our approach does not incorporate the phase offset $\vartheta(f, t_n)$ as it is unknown. In the following, we will show that thanks to the introduced virtual path, we can produce the significant cosine component in which the reference path interacts solely with the constant H_a in the aug-CSI power.

To proceed, we calculate the power of $H_{vi}(f, t_n)$, analyze each term sequentially, and derive the expressions of the principal components obtained through PCA. We define $H_a \triangleq A_a e^{j\phi_a}$, where A_a and ϕ_a are the constant magnitude and phase of the virtual path, then the power of $H_{1,2}(f, t_n)$ is expressed as

$$\begin{aligned} |H_{vi}(f, t_n)|^2 &= A_a^2 + \underbrace{\sum_{k \in \Omega_1(t_n)} A_k^2(f, t_n) + \sum_{i \in \Omega_2(t_n)} A_i^2(f, t_n)}_{(1)} \\ &\quad + \underbrace{\sum_{k, k' \in \Omega_1(t_n), k \neq k'} F(f, t_n, k, k') + \sum_{i, i' \in \Omega_2(t_n), i \neq i'} F(f, t_n, i, i')}_{(2)} + \sum_{k \in \Omega_1(t_n), i \in \Omega_2(t_n)} F(f, t_n, k, i) \\ &\quad + \underbrace{\sum_{k \in \Omega_1(t_n)} 2A_a A_k(f, t_n) \cos(\phi_k(f, t_n) + \phi_a) + \sum_{i \in \Omega_2(t_n)} 2A_a A_i(f, t_n) \cos(\phi_i(f, t_n) + \phi_a)}_{(3)}, \end{aligned} \quad (8)$$

where

$$\phi_k(f, t_n) = \frac{2\pi f}{c} l_k(t_n) + \sigma_k(t_n) + \vartheta(f, t_n). \quad (9)$$

In Equation 8, the term (1) barely changes. Comparing with the cosine terms in Equation 6, we observe a fundamental difference: in the default CSI power, all paths are intertwined with each other, making it difficult to extract pure components containing information from a single path. However, after introducing the virtual path H_a , as shown in Equation 8, each path can interact only with the constant H_a . Consequently, the term (3) in Equation 8 becomes a purely additive combination of individual path information, suggesting the possibility of extracting the desired reference path information from the aug-CSI power.

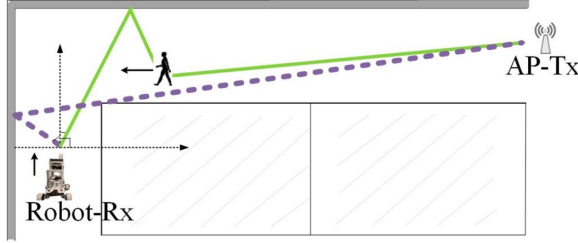


Fig. 5. Two dominant paths in the corner. Here, the purple dashed line representing the reference path, which undergoes only a single wall reflection, is the strongest path. The green solid line represents the dominant human-reflected path.

3.3 Reference Path Extraction

3.3.1 Dominant Path Analysis in Corner Scenarios. In this work, we utilize a reference path, denoted as $H_r(f, t_n)$, for two key purposes. First, subtracting it from the aug-CSI ensures that the dominant human-reflected path emerges as the primary component in the residual aug-CSI, thereby facilitating its subsequent extraction. Second, the reference path is used to compensate for the phase offset in the extracted dominant human-reflected path. To clarify the process of extracting the reference path from the aug-CSI, we begin by analyzing the paths in $\Omega_1(t_n)$ and $\Omega_2(t_n)$, see Appendix 2 for details. As illustrated in Figure 5, our analysis reveals that in corner scenarios, there are two dominant paths: a purple dashed reference path that only involves robot motion, and a green solid dominant human-reflected path that includes one reflection off the human.

We now have identified two dominant paths in the raw CSI in the corner scenario: the reference path $H_r(f, t_n)$ and the dominant human-reflected path $H_u(f, t_n)$. Following this analysis and based on Equation 8, we can derive an alternative expression for the aug-CSI power,

$$\begin{aligned}
 |H_{vi}(f, t_n)|^2 &= A_a^2 + \underbrace{\sum_{k \in \Omega_1(t_n)} A_k^2(f, t_n) + \sum_{k \in \Omega_2(t_n)} A_k^2(f, t_n)}_{(1)} \\
 &\quad + \underbrace{\sum_{k, k' \in \Omega_1(t_n), k \neq k'} F(f, t_n, k, k') + \sum_{i, i' \in \Omega_2(t_n), i \neq i'} F(f, t_n, i, i')}_{(2)} + \sum_{k \in \Omega_1(t_n), i \in \Omega_2(t_n)} F(f, t_n, k, i) \\
 &\quad + \underbrace{\sum_{k \in \Omega_1(t_n), k \neq r} 2A_a A_k(f, t_n) \cos(\phi_k(f, t_n) + \phi_a)}_{(3)} + \sum_{i \in \Omega_2(t_n), i \neq u} 2A_a A_i(f, t_n) \cos(\phi_i(f, t_n) + \phi_a) \\
 &\quad + \underbrace{2A_a A_r(f, t_n) \cos(\phi_r(f, t_n) + \phi_a)}_{(4)} + \underbrace{2A_a A_u(f, t_n) \cos(\phi_u(f, t_n) + \phi_a)}_{(5)} + \\
 &\quad + 2A_a A_r(f, t_n) \cos(\phi_r(f, t_n) + \phi_a) + 2A_a A_u(f, t_n) \cos(\phi_u(f, t_n) + \phi_a).
 \end{aligned} \tag{10}$$

Examining the current aug-CSI power expression in Equation 10 reveals that it is feasible to extract components associated with the reference path, namely term (4). It is worth noting that term (5) will be employed in a subsequent module dedicated to robot motion and phase offset compensation, while in this section, our focus remains on the reference path in term (4). Furthermore, we observe that the cosine component of paths in $\Omega_1(t_n)$, denoted as $w_k(f, t_n) = \cos(\phi_k(f, t_n) + \phi_a)$, can be decomposed into: $\cos(\phi_k(f, t_n) + \phi_a) = \cos \phi_a \cos(\phi_k(f, t_n)) -$

$\sin \phi_a \sin(\phi_k(f, t_n))$. Then each term of (3), i.e., $2A_a A_k(f, t_n) \cos(\phi_k(f, t_n) + \phi_a)$, including the reference path marked with r , can be expressed as a linear combination of two uncorrelated components:

$$2A_a A_k(f, t_n) \cos(\phi_k(f, t_n) + \phi_a) = 2A_a A_k(f, t_n) \cos \phi_a \cos(\phi_k(f, t_n)) - 2A_a A_k(f, t_n) \sin \phi_a \sin(\phi_k(f, t_n)). \quad (11)$$

Note that the statistical uncorrelation between the terms $\cos(\phi_k(f, t_n))$ and $\sin(\phi_k(f, t_n))$ arises from the fact that $\phi_k(f, t_n)$ is uniformly distributed over $[0, 2\pi]$.

3.3.2 Extraction of Reference Path's Components. In this subsection, we investigate the mechanism behind the extraction of the reference path from the aug-CSI power using PCA and validate the conditions that ensure its successful extraction. Recall that the reference path, which experiences a single reflection from the wall to the moving robot, typically has an amplitude stronger than other paths in $\Omega_1(t_n)$ and $\Omega_2(t_n)$ —these being the paths that experience multiple reflections off walls and humans. Within $\Omega_1(t_n)$, the reference path dominates, being the only significant contribution, while other multipath components are negligible. For paths in $\Omega_2(t_n)$, which all involve human body reflections before reaching the mobile robot. Thus, extracting the reference path fundamentally involves assessing the linear correlation between the reference path and the human-reflected paths. To that end, we go through a verification to show that the component $w_r(f, t_n) = \cos(\phi_r(f, t_n) + \phi_a)$ associated with the reference path exhibits zero linear correlation with any component $w_i(f, t_n) = \cos(\phi_i(f, t_n) + \phi_a)$ associated with paths in $\Omega_2(t_n)$. See Appendix 3 for details.

After verifying the zero linear correlation between the reference path and human-reflected paths in $\Omega_2(t_n)$, we further explore how to extract components of the reference path using PCA. According to Equation 11, the cosine term of the reference path in the aug-CSI power given in Equation 10 can be written as

$$2A_a A_r(f, t_n) \cos(\phi_r(f, t_n) + \phi_a) = 2A_a A_r(f, t_n) \cos \phi_a \cos(\phi_r(f, t_n)) - 2A_a A_r(f, t_n) \sin \phi_a \sin(\phi_r(f, t_n)). \quad (12)$$

We now proceed with our analysis by applying an important property of PCA, presented as Property 1 in Appendix 1 (A Brief Primer on PCA). Considering that the reference path is the strongest path, the two components $2A_a A_r(f, t_n) \cos \phi_a \cos(\phi_r(f, t_n))$ and $-2A_a A_r(f, t_n) \sin \phi_a \sin(\phi_r(f, t_n))$, are identified as the dominant components during the PCA process³. This dominance arises because A_a , which is under our control, can be set much larger than the magnitude of any other path, and the reference path carrying A_r is inherently the strongest path. When considering the linear superposition of such components from all paths in the scenario, the coefficients (like $2A_a A_r \cos \phi_a$ and $2A_a A_r \sin \phi_a$) correspond to C_i in **Property 1** (Appendix 1), while the trigonometric terms (like $\cos(\phi_r(f, t_n))$ and $\sin(\phi_r(f, t_n))$) correspond to the functions x_i . According to **Property 1**, since these two components $2A_a A_r(f, t_n) \cos \phi_a \cos(\phi_r(f, t_n))$ and $-2A_a A_r(f, t_n) \sin \phi_a \sin(\phi_r(f, t_n))$ have the largest coefficients, they emerge as the dominant components in the PCA process. Their linear combinations along the f dimension form the first two largest principal components, denoted as $\mathbf{z}_1, \mathbf{z}_2 \in \mathbb{R}^{1 \times N}$, respectively. This dominance is ensured if $A_a \sin \phi_a$ and $A_a \cos \phi_a$ are significantly larger than $A_k(f, t_n)$ for all $k \in \Omega_1(t_n)$ and than $A_i(f, t_n)$ for all $i \in \Omega_2(t_n)$. Therefore, we recommend setting A_a to be 1 ~ 10 times the amplitude of the strongest path in the environment, which ensures that the interaction terms between the virtual path and reference path emerge as the dominant components in PCA, while avoiding excessive suppression of other path information. However, in practical experiments, it can be challenging to precisely measure the amplitude of a single strongest physical path. Instead, we typically use 1-3 times the maximum amplitude observed in the collected CSI data (which represents the superposition of all path amplitudes) to ensure this theoretical requirement is met. When these conditions hold, the variances of $2A_a A_r(f, t_n) \cos \phi_a \cos(\phi_r(f, t_n))$ and $-2A_a A_r(f, t_n) \sin \phi_a \sin(\phi_r(f, t_n))$ will always be larger than other path's components in Equation 8. To achieve this, we set the values of $A_a \sin \phi_a$ and $A_a \cos \phi_a$ to be substantially larger than the maximum single-path magnitude. Furthermore, by setting

³The PCA is applied to our aug-CSI power matrix with dimensions $N \times K$. Recall that N is the number of total samples and K is the total number of subcarriers.

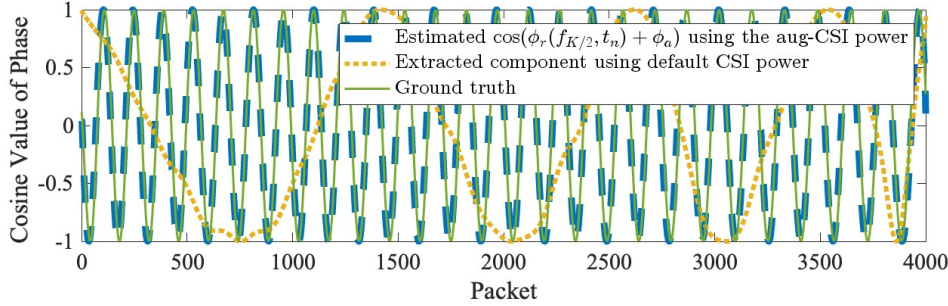


Fig. 6. Comparison of the estimated $\phi_r(f_{K/2}, t_n)$ using our aug-CSI power, the component extracted from the default CSI power, and the ground truth.

$\phi_a = \pi/4$, we ensure that $\sin \phi_a = \cos \phi_a$, which guarantees both sine and cosine components related to the reference path have equal strength in the PCA decomposition. This prevents any weaker paths from interfering with these two primary components. Therefore, the two uncorrelated principal components, \mathbf{z}_1 and \mathbf{z}_2 , will have nearly equal variances (or eigenvalues) when a sufficient number of samples are available.

3.3.3 Reference Path Construction. We are now ready to construct the reference path using the principal components \mathbf{z}_1 and \mathbf{z}_2 obtained above. Specifically, we aim to recover the two terms, i.e., $2A_a A_r(f, t_n) \cos \phi_a \cos(\phi_r(f, t_n))$ and $-2A_a A_r(f, t_n) \sin \phi_a \sin(\phi_r(f, t_n))$, of the reference path in the original frequency dimension from \mathbf{z}_1 and \mathbf{z}_2 . To that end, we project the principal components back using their corresponding eigenvectors. Let $\mathbf{v}_1, \mathbf{v}_2 \in \mathbb{R}^{K \times 1}$ be the two eigenvectors corresponding to \mathbf{z}_1 and \mathbf{z}_2 , respectively. We have $\mathbf{X}_1 = \mathbf{v}_1 \cdot \mathbf{z}_1 \in \mathbb{R}^{K \times N}$ and $\mathbf{X}_2 = \mathbf{v}_2 \cdot \mathbf{z}_2 \in \mathbb{R}^{K \times N}$ where \cdot denotes the vector multiplication operation. These reconstructed matrices \mathbf{X}_1 and \mathbf{X}_2 represent $2A_a A_r(f, t_n) \cos \phi_a \cos(\phi_r(f, t_n))$ and $-2A_a A_r(f, t_n) \sin \phi_a \sin(\phi_r(f, t_n))$ across all frequencies f (i.e., K subcarriers) and time samples t_n (i.e., N samples). We then obtain the CSI of the reference path $A_r(f, t_n) \cos(\phi_r(f, t_n)) - jA_r(f, t_n) \sin(\phi_r(f, t_n))$ in the original frequency dimension by combining the two reconstructed matrices \mathbf{X}_1 and \mathbf{X}_2 and removing the known values of H_a and ϕ_a .

We recall that the reference path CSI at f , defined in Equation 3, can be rewritten as

$$H_r(f, t_n) = A_r(f, t_n) e^{-j\phi_r(f, t_n)}, \quad (13)$$

where $\phi_r(f, t_n) = \frac{2\pi f}{c} l_r(t_n) + \sigma_r(t_n) + \vartheta(f, t_n)$. We remark that the estimated phase of the reference path happens to retain the phase offset induced by hardware impairments (i.e., $\vartheta(f, t_n)$). This, as we will show later, enables the effective compensation of the phase offset from the dominant human-reflected path extracted in the RMPOC algorithm.

We now evaluate the accuracy of our reference path extraction approach using simulation data generated by the ray-tracing software Wireless InSite [1]. Our dataset comprises 4000 CSI data, each with $K = 30$ subcarriers centered at $f_c = 5.32\text{GHz}$, collected with a temporal sampling frequency of 1kHz when an Rx moves towards a corner at a speed of 1 m/s. As shown in Figure 6, the close match between the estimated $\cos(\phi_r(f_{K/2}, t_n))$ from the aug-CSI power using our approach and the ground truth confirms the effectiveness of the proposed reference path extraction method. By contrast, the component extracted from the default CSI power fails to reveal any meaningful path information, underscoring the efficacy of our aug-CSI power.

3.4 Dominant Human-reflected Path Extraction and RMPOC Algorithm

In this section, our goal is to remove the robot motion effects and leverage the extracted reference path $H_r(f, t_n)$ to compensate the phase offset from the dominant human-reflected path for accurate human motion detection.

Previous radar-based research [[52]] introduced the concept of using a reference path to isolate and remove robot-induced motion from human-reflected signal components. This inspires a potential approach for mitigating receiver motion in our setting by dividing $H(f, t_n)$ by the reference path $H_r(f, t_n)$. However, this method is not directly applicable to our problem, as $H(f, t_n)$ comprises multiple superimposed paths—each influenced differently by the robot’s velocity due to their distinct AoAs in the CSI measurements. To overcome this WiFi-specific challenge, we introduce a systematic method for processing these dynamic path categories and present the RMPOC algorithm, formally described in Alg. 1.

To proceed, first review the dominant paths in $\Omega_1(t_n)$ and $\Omega_2(t_n)$ to clarify our approach to compensating the effects of robot motion. In $\Omega_1(t_n)$, the reference path $H_r(f, t_n)$ dominates while other paths with multiple reflections are negligibly weak, as shown in Figure 15. In $\Omega_2(t_n)$, the dominant human-reflected path $H_u(f, t_n)$, shown in green in Figure 16a, travels from the transmitter to the human target and then to the robot with a single wall reflection. All other multi-reflection paths in this set are substantially weaker. Notably, because the dominant human-reflected path in $\Omega_2(t_n)$ undergoes two reflection attenuations in total, we need to remove paths in $\Omega_1(t_n)$ that are stronger than the dominant human-reflected path. In other words, we need to ensure that among all paths in $\Omega_1(t_n)$ and $\Omega_2(t_n)$, the dominant human-reflected path is the strongest, and then we have the opportunity to extract it using our aug-CSI power.

Based on this analysis, Alg. 1 specifies how to: 1) remove dynamic paths with single wall reflection in $\Omega_1(t_n)$ from $H_{vi}(f, t_n)$, 2) extract the dominant human-reflected path using our aug-CSI power, and 3) compensate for the robot’s motion and the phase offset in the dominant human-reflected path.

Algorithm 1 Robot Motion and Phase Offset Compensation (RMPOC) Algorithm

Require: $H_{vi}(f, t_n)$, $H_r(f, t_n)$, robot velocities.

Ensure: Cleared CSI data containing only human motion.

- 1: Subtract the reference path $H_r(f, t_n)$ from the aug-CSI $H_{vi}(f, t_n)$ and obtain the residual aug-CSI $H_{res}(f, t_n)$ with Equation 14;
 - 2: Obtain the power of the residual aug-CSI and extract the dominant human-reflected path $H_u(f, t_n)$, as shown in Equation 15;
 - 3: For $n = 1$ to N :
 - 4: Build $H''_u(f, t_n)$ following Equations 17, 18, and 23;
 - 5: End;
 - 6: Remove the impact of amplitude and obtain the cleaned CSI $H'''_u(f, t_n)$ following Equation 20;
 - 7: End;
-

3.4.1 Removal of dynamic paths with single wall reflection in $\Omega_1(t_n)$. To eliminate from artifical CSI $H_{vi}(f, t_n)$ the dynamic paths in $\Omega_1(t_n)$ that are stronger than the dominant human-reflected path, we first eliminate the reference path and obtain the residual artifical CSI. Mathematically,

$$\begin{aligned} H_{res}(f, t_n) &\triangleq H_{vi}(f, t_n) - H_r(f, t_n) \\ &= H_a + e^{-j\vartheta(f, t_n)} \sum_{k \in \Omega_1(t_n), k \neq r} A_k(f, t_n) e^{-j\frac{2\pi f}{c}l_k(t_n) - j\sigma_k(t_n)} + e^{-j\vartheta(f, t_n)} \sum_{i \in \Omega_2(t_n)} A_i(f, t_n) e^{-j\frac{2\pi f}{c}l_i(t_n) - j\sigma_i(t_n)}. \end{aligned} \quad (14)$$

Although other paths exist within $\Omega_1(f, t_n)$, their amplitudes are significantly weaker compared to the dominant human-reflected path $H_u(f, t_n)$. Moreover, they exhibit minimal linear correlation with $H_u(f, t_n)$, which can be established using similar analysis presented in Section 3.3. Consequently, the dominant human-reflected path $H_u(f, t_n)$ emerges as the strongest component in the residual artifical CSI $H_{res}(f, t_n)$ and other paths pose negligible interference to the subsequent extraction of the dominant human-reflected path.

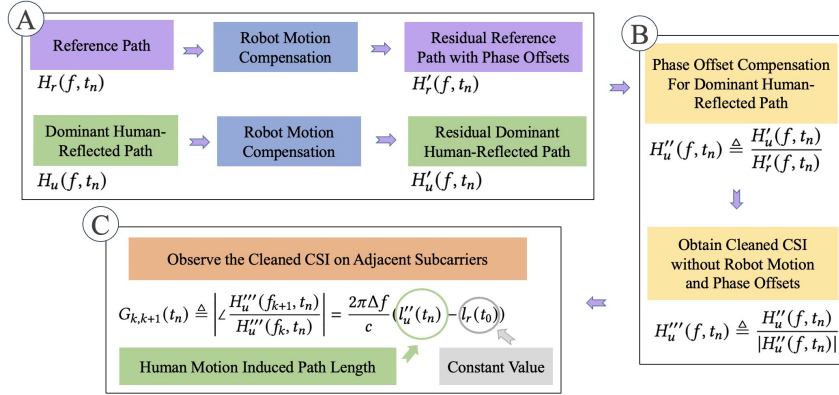


Fig. 7. Data Processing Workflow.

3.4.2 Extract the dominant human-reflected path $H_u(f, t_n)$ using PCA. We now apply PCA to the power of the residual aug-CSI H_{res} for frequency dimension reduction and principal component extraction, obtaining the first two principal components \mathbf{z}_3 and \mathbf{z}_4 . Following the same approach as in Section 3.3.3, we restore these two principal components \mathbf{z}_3 and \mathbf{z}_4 to their original frequency dimensions, obtaining $2A_a A_u(f, t_n) \cos \phi_a \cos(\phi_u(f, t_n))$ and $-2A_a A_u(f, t_n) \sin \phi_a \sin(\phi_u(f, t_n))$ across k subcarriers with $\phi_u(f, t_n) = \frac{2\pi f}{c} l_u(t_n) + \sigma_u(t_n) + \vartheta(f, t_n)$. Subsequently, we can reconstruct the dominant human-reflected path given by

$$H_u(f, t_n) = A_u(f, t_n) e^{-j \frac{2\pi f}{c} l_u(t_n) - j \sigma_u(t_n) - j \vartheta(f, t_n)}. \quad (15)$$

As illustrated in Figure 4, after obtaining principal components through two consecutive PCA operations, we have constructed the reference path and dominant human-reflected path. Our next focus is on leveraging these two paths to obtain cleaned CSI that is free from robot motion effects and phase offsets. Figure 7 presents our new data processing pipeline. In the following sections, we will elaborate on Steps A and B to acquire the cleaned CSI.

3.4.3 Compensation of robot's speed $v_m(t_n)$ and the phase offset $\vartheta(f, t_n)$ in $H_u(f, t_n)$. Recall that our objective is to detect human motion, which is reflected in the path length term $l_u(t_n)$ appearing in the phase of the dominant human-reflected path, as defined in Equation 15. Nevertheless, the PLCR of the dominant human-reflected path influenced by both the movements of both robot and human target, and is further obscured by the random phase offset. To obtain cleaned CSI that exclusively captures human-induced motion, it is necessary to compensate for the effects of both the robot's motion and the phase offset. Our first objective is to compensate for the robot motion. To proceed, we examine how the path length $l_u(t_n)$ in $H_u(f, t_n)$ is influenced by both human and robot motion and obtain the following expression

$$l_u(t_n) = l_u(t_0) + \sum_{q=1}^n \frac{v_p(t_q) \Delta t}{\sin \theta_u(t_q)} + L_{Tx}(t_n) + \sum_{q=1}^n v_m(t_q) \Delta t \cos \theta_u(t_q), \quad (16)$$

where $L_{Tx}(t_n)$ represents the path length changes between the human and Tx due to human motion, independent of robot movement.

As shown in Equation 16, to compensate for the robot motion, we need to know the values of robot velocity $v_m(t_n)$ and the AoA $\theta_u(t_n)$ of the extracted human-reflected path. The robot's onboard sensors provide direct measurements of $v_m(t_n)$. To estimate the AoA values, we apply the method proposed in [25] to the raw CSI measurements, which yields the potential AoAs of the dominant propagation paths. We then designate the AoA corresponding to the strongest path as the AoA of the extracted reference path, denoted by $\theta_m(t_n)$. Similarly, the AoA associated with the second strongest path is taken as the AoA of the dominant human-reflected path (i.e.,

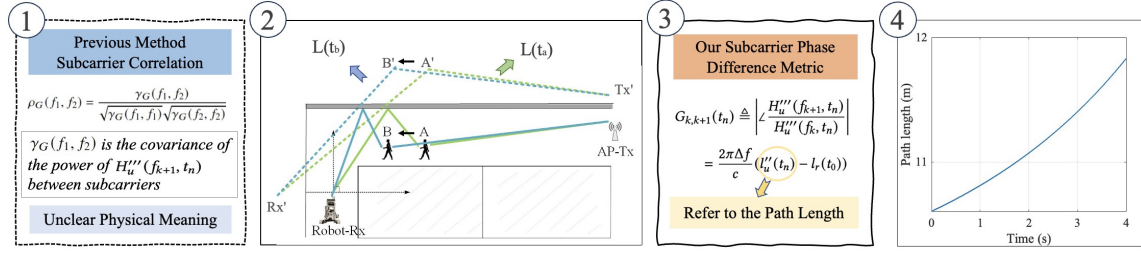


Fig. 8. Comparison between previous subcarrier correlation metric and our approach. Our subcarrier phase difference metric directly reflects the path length variation ($L(t_a)$ to $L(t_b)$) during target movement (point A to point B), while the traditional metric ρ_G [21] lacks such physical interpretation.

$\theta_u(t_n)$). We now can compensate for the robot motion in $l_u(t_n)$ and obtain:

$$H'_u(f, t_n) \triangleq e^{-j\vartheta(f, t_n)} A_u(f, t_n) e^{-j\frac{2\pi f}{c} l'_u(t_n) - j\sigma_u(t_n)}, \quad (17)$$

where $l'_u(t_n) = l_u(t_n) - \sum_{q=1}^n v_m(t_q) \Delta t \cos \theta_u(t_q)$. Our second objective is to compensate the phase offset $\vartheta(f, t_n)$. For this purpose, we can leverage the reference path $H_r(f, t_n)$, which contains only robot motion and phase offset. We first remove the robot motion in the reference path using a similar method as in Equation 17 and obtain

$$H'_r(f, t_n) \triangleq \frac{H_r(f, t_n)}{A_r(f, t_n) e^{-j\frac{2\pi f}{c} l'_r(t_n)}} = e^{-j\frac{2\pi f}{c} l_r(t_0) - j\sigma_r(t_n) - j\vartheta(f, t_n)}, \quad (18)$$

where $l'_r(t_n) = \sum_{q=1}^n v_m(t_q) \cos \theta_m(t_q) \Delta t$. Now by dividing H'_u by H'_r , we can compensate the phase offset and obtain

$$H''_u(f, t_n) \triangleq \frac{H'_u(f, t_n)}{H'_r(f, t_n)} = A_u(f, t_n) e^{-j\frac{2\pi f}{c} (l''_u(t_n) - l_r(t_0)) - j(\sigma_u(t_n) - \sigma_r(t_n))}, \quad (19)$$

where $l''_u(t_n) = l_u(t_0) + \sum_{q=1}^n \frac{v_p(t_q) \Delta t}{\sin \theta_u(t_q)} + L_{Tx}(t_n)$.

Finally, to exclude the impact of amplitude changes induced by the robot motion, we normalize H''_u and obtain

$$H'''_u(f, t_n) \triangleq \frac{H''_u(f, t_n)}{|H''_u(f, t_n)|}. \quad (20)$$

The resulting $H'''_u(f, t_n)$ captures phase variations induced by human motion, while effectively eliminating the effects of robot motion and phase offsets. This cleaned CSI data can be used to accurately detect human proximity around corners as if the robot kept static. We remark that as shown in the subsequent subsection, the term $\sigma_u(t_n) - \sigma_r(t_n)$ in the phase can be effectively mitigated when computing the phase difference between adjacent subcarriers.

3.5 Human Proximity Detection via Subcarrier Phase Difference

With the cleaned CSI data, existing WiFi-based proximity detection algorithms, originally designed for stationary transceivers, can be readily applied. For example, the method proposed in [21] estimates proximity by analyzing the subcarrier correlation, as the target moves closer to the receiver. However, as demonstrated in Figure 8① and ②, this approach does not establish a precise quantitative relationship between subcarrier correlation and the actual distance between the human and the receiver. Following Step C shown in Figure 7, we now focus on implementing proximity detection using the cleaned CSI. Our goal is to establish a direct relationship between human motion and the path length variations embedded in the phase of cleaned CSI. Leveraging CornerSense's

ability to isolate the CSI of the dominant human-reflected path, we introduce a new and more effective metric that directly and accurately measures path length variations caused by human motion. The theoretical analysis and corresponding experimental validation of this approach are presented below.

We first note that in the phase of $H_u'''(f, t_n)$, the path length change caused by human movement is characterized by the change of $l_u''(t_n)$. However, directly determining the absolute change of $l_u''(t_n)$ from the phase of $H_u'''(f, t_n)$ is difficult due to the large phase values induced by the large value of subcarrier frequency f , resulting the ambiguity caused by the unknown number of 2π phase wraps. Fortunately, we have obtained the phase of $H_u'''(f, t_n)$ on M subcarriers, enabling the examination of the change of $l_u''(t_n)$ from the perspective of subcarrier spacing. Because the subcarrier spacing is much smaller than the subcarrier frequency, the phase difference between adjacent subcarriers is guaranteed to remain within a 2π range, given that the total displacement distance of the robot is limited. This avoids phase wrapping and allows for unambiguous estimation of the path length term $l_u''(t_n) - l_r(t_0)$. Although $l_r(t_0)$ is unknown, it remains constant over time. Therefore, by tracking changes in the term $l_u''(t_n) - l_r(t_0)$, we can effectively infer the path length change induced by human motion. In light of this important observation, we define a new metric, termed the subcarrier phase difference, as follows

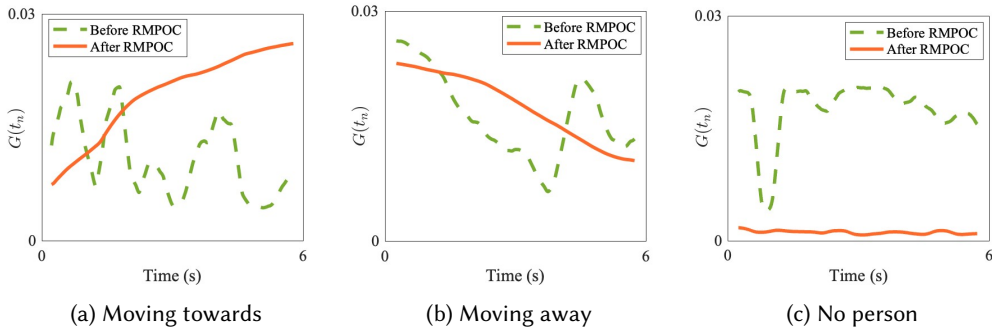
$$G_{k,k+1}(t_n) \triangleq \left| \angle \frac{H_u'''(f_{k+1}, t_n)}{H_u'''(f_k, t_n)} \right| = \frac{2\pi\Delta f}{c} (l_u''(t_n) - l_r(t_0)). \quad (21)$$

We remark that the phase term $\sigma_u(t_n) - \sigma_r(t_n)$ is removed when calculating the subcarrier phase difference, eliminating its impact on human proximity detection. Averaging $G_{k,k+1}(t_n)$ over $K - 1$ adjacent subcarrier pairs, we have

$$G(t_n) \triangleq \frac{1}{K-1} \sum_{k=1}^{K-1} G_{k,k+1}(t_n). \quad (22)$$

When multiple Rx antennas are used, $G(t_n)$ can be further averaged across the CSI streams from different antennas to enhance robustness. Finally, the resulting $G(t_n)$ is smoothed using a moving average filter to reveal its trends over time, which reflects the path length change induced only by human motion. We now examine the relationship between the trend of $G(t_n)$ and the human's movement, specifically, approaching the corner, moving away from it, or being absent. We first note that when a person approaches the corner, the total path length increases. For instance, as shown in Figure 8②, as a person moves from point A to B, the path length increases from the green dashed line to the longer blue dashed line. We further confirm this conclusion using simulation, with the results depicted in Figure 8④. In our simulation setup, we consider a corner with 2m-wide corridors. The Tx is placed 6m from the corner on one side, and the Rx is positioned 2m from the corner on the other side of the corner. The target moves toward the corner at a speed of 1m/s. Starting from 4m away, we observe a continuous increase in the path length as the target approaches the corner. This confirms that the value of $G(t_n)$ increases as the person moves closer to the corner. We further conclude that $G(t_n)$ decreases when the human moves away from the corner. Furthermore, when no person is present around the corner, the dominant human-reflected path is absent. Consequently, applying our method to extract the dominant human-reflected path yields a signal component that reflects only the robot's own motion. After compensating for the robot's velocity and phase offset, this results in no observable change in path length—i.e., a stable $G(t_n)$. We remark that for any WiFi systems with small enough subcarrier spacing Δf , $G(t_n)$ maintains the monotonic behavior when $l_u''(t_n) - l_r(t_0) \in (0, \frac{c}{\Delta f})$, ensuring effective distance detection within typical indoor environments.

Figure 9 plots the curves of $G(t_n)$ for three distinct cases, i.e., moving towards the corner, moving away from the corner, and no person presence. As a comparison, we also compute the subcarrier phase difference for the extracted dominant human-reflected path, i.e., $H_u(f, t_n)$, in which the robot motion and phase offset compensation have not been compensated. As observed in Figure 9, the green dashed lines in all three cases exhibit complex and ambiguous patterns, making it infeasible to extract any meaningful information related to human motion. This observation can be attributed to two main reasons. First, the extracted dominant human-reflected path contains

Fig. 9. The curves of $G(t_n)$ for different human motion cases.

both robot motion and human motion, resulting in complex path length variations. The path length variations induced by the robot's motion may occasionally counteract those caused by human movement, or even produce trends that contradict the actual human motion. Second, random phase offsets could mask these movements, further complicating the interpretation of the phase variations. In contrast, the subcarrier phase differences, after applying our RMPOC algorithm to compensate for the robot's motion and phase offset in the extracted dominant human-reflected path, exhibit clear and expected patterns, as shown in Figure 9. Specifically, the orange solid line rises when a person approaches the corner, falls when moving away, and remains stable when no one is present. The results align well with our analysis of the relationship between the trend of $G(t_n)$ and human movement, validating the efficacy of the proposed RMPOC algorithm and the effectiveness of the proposed subcarrier phase difference metric.

4 IMPLEMENTATION AND EVALUATION

To evaluate the effectiveness and robustness of CornerSense in proximity detection around corners on mobile robots, we conduct experiments in three groups with nine distinct corner scenarios under four different walking patterns. In each scenario, we design various tests with the target moving in different directions and ranges.

4.1 Experiment Settings

Data Collection:

We use mini PCs equipped with Intel 5300 network interface cards (NICs) operating on the IEEE 802.11n standard to conduct these experiments. The NICs are configured to use Channel 64, which has a center frequency of 5.32 GHz and a bandwidth of 20 MHz. These PCs serve as the Tx and Rx, with both equipped with omnidirectional antennas to ensure uniform signal coverage in all directions, as illustrated in Figure 10. Specifically, the Tx uses a single omnidirectional antenna and is positioned at a height of 1.5 meters, broadcasting packets at a rate of 1000 Hz using packet injection mode. The Rx is equipped with three omnidirectional antennas and is mounted on a Scout Mini robot [4], which moves at a constant speed. The Rx employs the 5300 CSI Tool [19] to extract and collect CSI data, which includes information on 30 subcarriers for each antenna, from each received packet. The collected CSI data is then analyzed on a computer powered by an Intel i7 processor using MATLAB.

Evaluation setup: We recruited twelve volunteers—six males and six females aged between 20 and 30 years, with heights ranging from 160 to 185 cm—to participate in the experiments. All participants were informed that the collected data would be used solely for proximity detection and localization analysis, and their identities were anonymized in the dataset. During the experiments, participants wore face masks and their facial features were masked in all documentation photos to protect their privacy. In the first group, participants were instructed to

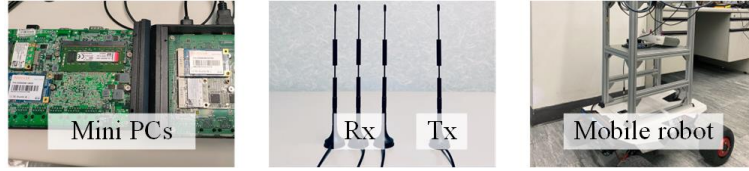


Fig. 10. Experimental Devices

walk naturally at typical daily walking speeds across three distinct scenarios: a corridor corner, a staircase corner, and a room entrance corner, as depicted in the first row of Figure 11. In the second group, participants were asked to adopt various walking patterns randomly, including walk naturally, walking with a backpack, walking while making phone call, and walking while holding objects. The experiments were conducted in three new scenarios: a corridor corner, an elevator corner, and a room entrance corner, as shown in the second row of Figure 11. In the third group, participants were assigned random walking patterns, and the experiments were conducted in more complex corner scenarios. These scenarios included a corner with multiple seated occupants, a corner with standing occupants, and a corner with additional static objects, as illustrated in the third row of Figure 11.

Data were recorded for two specific regions: R_1 (1-2 m away from the corner) and R_2 (more than 2 m away from the corner) while the participants approached and departed from the corner. At the same time, the robot moved towards the corner from another side of the corner at a consistent speed of 0.2 m/s. Additionally, to establish a baseline for comparison, we also collected CSI data in scenarios where the corner was unoccupied by any person. For each group, we conducted 20 repetitions of each experiment under five different conditions (moving towards in R_1 , moving away in R_1 , moving towards in R_2 , moving away in R_2 , and no person) across three scenarios, resulting in 300 data points (20 repetitions \times 5 conditions \times 3 scenarios) per group. In total, we collected 900 data points across all three groups. In addition, to calibrate the algorithm's threshold, we collected an additional 50 data points from the room entrance corner and staircase corner, including 10 data points for approaching within R_1 range, 10 data points for approaching within R_2 range, 10 data points for moving away within R_1 range, 10 data points for moving away within R_2 range, and 10 data points for no person, to constitute the training dataset.

4.2 System Performance

In this subsection, the performance evaluation of CornerSense is conducted with a focus on the accuracy of proximity detection and region classification using our subcarrier phase difference metric $G(t_n)$. To establish a robust benchmark, we apply the algorithm proposed in [21] directly to the collected CSI measurements. For a comprehensive evaluation, we employ multiple performance metrics. In our system, we define a positive case as a scenario where a person is approaching the corner, while all other instances (no human presence or moving away) are classified as negative cases. In our balanced dataset, positive cases account for one-third of all samples. The true positive rate (TPR)/recall quantifies the proportion of actual approaching cases correctly identified, while the false positive rate (FPR) reflects the proportion of non-approaching cases incorrectly classified as approaching. Here, true positives (TP) refer to correctly identified approaching cases, and false positives (FP) are non-approaching cases incorrectly classified as approaching. Precision, defined as $TP/(TP+FP)$, measures the proportion of correct approaching predictions among all approaching predictions. The F1-score, calculated as $2 \times (Precision \times Recall) / (Precision + Recall)$, provides a balanced measure of the system's overall performance.

4.2.1 Proximity Detection. Taking into account the velocities of both the robot and human participants, we define a positive case of proximity detection as a scenario where a person is moving toward the corner. All other instances are classified as negative cases. To account for fluctuations in the subcarrier phase difference metric

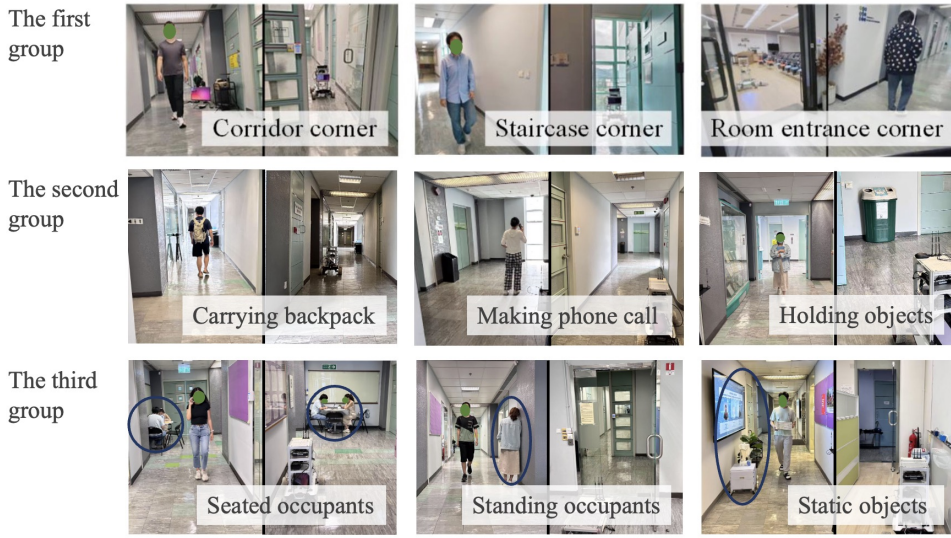


Fig. 11. Illustration of three groups of scenarios: the first group with three simple corners, the second group with different target behavior patterns, and the third group with different environmental configurations, where blue circles represent occupants or static objects.

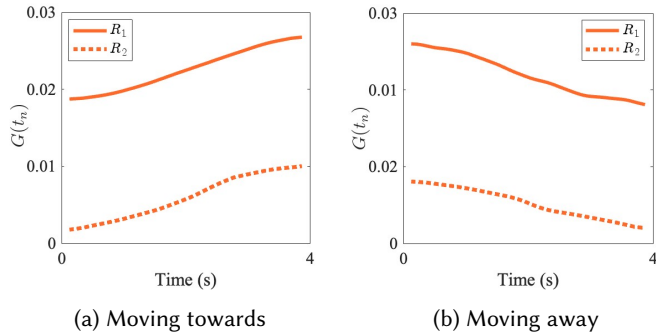


Fig. 12. The variation of the subcarrier phase difference metric $G(t_n)$ across various directions and regions.

induced by noise and other factors, we introduce a cumulative path length variation indicator, \mathbb{I}_g , defined as

$$\mathbb{I}_g \triangleq \frac{c}{2\pi\Delta f} \sum_{n=1}^N (G(t_n) - G(t_{n-1})) \approx \sum_{n=1}^N (l''_u(t_n) - l''_u(t_{n-1})). \quad (23)$$

The metric \mathbb{I}_g essentially represents the cumulative path length variation caused by human movement over time. Through comprehensive analysis of the training data, we empirically determined that $\mathbb{I}_g > 0.1$ achieves the highest TPR for detecting approaching targets. This threshold of 0.1 corresponds to a path length variation of 10 cm, which effectively balances the detection of meaningful human approach while mitigating false positives from minor movements, such as body sway. Although any positive threshold theoretically indicates an approaching target due to an increasing path length, setting the threshold to zero risks false positives from subtle motions that induce non-negligible path length changes. Tab. 1 summarizes the performance of CornerSense across nine different

corner scenarios in three groups. On average, CornerSense achieves consistent performance across all groups in human proximity detection, with TPR ranging from 95% to 96% and FPR maintained at 2% ~ 3%. Given that the proximity detection needs to distinguish between approaching scenarios versus both non-approaching and no-person scenarios, our dataset naturally follows a 1:2 ratio of positive to negative cases. Under this distribution, the system demonstrates robust precision of 94% ~ 95% and F1-scores of 94% ~ 96%. Specifically, Group 1 and Group 2 show slightly better performance with F1-scores of 95% ~ 96%, even with varying walking patterns of volunteers, while Group 3, which involves more complex scenarios with seated occupants and objects, maintains a robust F1-score of 94%.

Table 1. Performance of CornerSense in proximity detection for three groups.

Group 1				
	Corridor	Staircase	Room	Average
TPR ^{*1}	0.95	0.96	0.96	0.96
FPR	0.03	0.03	0.02	0.03
Precision	0.94	0.94	0.96	0.95
F1-score	0.94	0.95	0.96	0.95

Group 2				
	Corridor	Elevator	Room	Average
TPR	0.97	0.96	0.96	0.96
FPR	0.02	0.03	0.02	0.02
Precision	0.96	0.94	0.96	0.95
F1-score	0.97	0.95	0.96	0.96

Group 3				
	Seated Occ. ^{*2}	Standing Occ.	With Obj. ^{*3}	Average
TPR	0.95	0.96	0.95	0.95
FPR	0.04	0.02	0.03	0.03
Precision	0.92	0.96	0.94	0.94
F1-score	0.93	0.96	0.94	0.94

*1: TPR = TPR (Recall); *2: Occ. = Occupants; *3: Obj. = Objects

Table 2. Performance of CornerSense in region classification for three groups.

Group 1				
	Corridor	Staircase	Room	Average
TPR	0.94	0.95	0.95	0.95
FPR	0.03	0.03	0.03	0.03
Precision	0.97	0.97	0.97	0.97
F1-score	0.95	0.96	0.96	0.96

Group 2				
	Corridor	Elevator	Room	Average
TPR	0.96	0.95	0.94	0.95
FPR	0.03	0.03	0.04	0.03
Precision	0.97	0.97	0.96	0.97
F1-score	0.96	0.96	0.95	0.96

Group 3				
	Seated Occ.	Standing Occ.	With Obj.	Average
TPR	0.93	0.95	0.94	0.94
FPR	0.04	0.03	0.04	0.04
Precision	0.96	0.97	0.96	0.96
F1-score	0.94	0.96	0.95	0.95

4.2.2 Region Classification. In this evaluation, we further challenge our framework to see whether it can distinguish whether the human proximities are within the region R_1 or R_2 . This evaluation is motivated by our observation that, although the trends of $G(t_n)$ are consistent when a human approaches the corner from different regions, the exact values vary across regions. This phenomenon is illustrated in Figure 12. Considering that the approaching human within R_1 can lead to a higher chance of collisions, we define a positive case as a person moving within R_1 . All other scenarios are classified as negative cases. We further define a threshold T_R such that a case is considered positive if the minimum value of $\frac{f}{2\pi\Delta f}G(t_n) \approx l''_u(t_n) - l''_u(t_0)$ is larger than T_R . When the minimum value of $l''_u(t_n) - l''_u(t_0)$ exceeds T_R , it indicates that even the farthest position during human movement remains within the range R_1 , thereby ensuring that the entire human motion trajectory is confined within the range R_1 . Analysis of the training dataset revealed that $T_R = 0.85$ yielded the highest TPR. Based on this observation, we selected this threshold value $T_R = 0.85$ for our system implementation. Tab. 2 presents the

performance of region classification within the range R_1 . The results are organized into three groups with different classification scenarios. Group 1 and Group 2 focus on different indoor environments (corridors, staircases, elevators, and rooms), with Group 2 additionally considering various walking patterns of humans, both achieving excellent performance with a TPR of 95% and FPR of 3%. Since region classification specifically distinguishes between humans in R_1 versus R_2 regions when human presence is detected, the dataset naturally contains an equal distribution of samples between these two regions (1:1 positive-to-negative ratio). Under this balanced distribution, these groups demonstrate strong precision of 97% and F1-scores of 96%. Group 3, which addresses more challenging corner scenarios involving seated or standing pedestrians and additional obstacles, maintains robust performance with a TPR of 94%, FPR of 4%, precision of 96%, and F1-score of 95%. These comprehensive results demonstrate CornerSense's robust capability to accurately classify human proximity within different environmental contexts and under various practical scenarios.

4.2.3 Baseline. For comparison, we applied the proximity detection algorithm from [21] to our collected CSI measurements under simple corner scenarios (Group 1 in Tab. 1). We set the proximity detection threshold to 0.13 and the region classification threshold to 0.5 to optimize the baseline's performance in our experimental evaluation. Specifically, a threshold of 0.13 is used for proximity detection: a cumulative increase in subcarrier correlation over consecutive time samples exceeding this value indicates a target moving toward the corner. The region classification threshold of 0.5 determines the presence of a target within range R_1 ; this is confirmed when the minimum subcarrier correlation across all samples exceeds the threshold. For comparison, we applied the proximity detection algorithm from [21] to our collected CSI measurements under simple corner scenarios (Group 1 in Tab. 1). We set the proximity detection threshold to 0.13 and the region classification threshold to 0.5 to optimize the baseline's performance in our experimental evaluation. Specifically, a threshold of 0.13 is used for proximity detection: a cumulative increase in subcarrier correlation over consecutive time samples exceeding this value indicates a target moving toward the corner. The region classification threshold of 0.5 determines the presence of a target within range R_1 ; this is confirmed when the minimum subcarrier correlation across all samples exceeds the threshold. As shown in Figure 13(1), using the method from [21], no distinguishable correlation patterns can be observed among the moving towards, moving away, and no-person scenarios. This is primarily due to the continuous robot movement, which makes the subcarrier correlation unable to effectively reflect the target's motion. In contrast, our CornerSense in Figure 13(2) demonstrates reasonable metric variations across all three scenarios, clearly distinguishing between different target states. As shown in Tab. 3, while the baseline achieved reasonable TPR performance (though still marginally lower than CornerSense), its overall effectiveness was significantly compromised by high false positive rates. For proximity detection, the FPR was 46% (approximately 15.3 times higher than CornerSense), resulting in a low precision of 48% and F1-score of 61%. The performance degradation was even more pronounced in region classification, where the FPR reached 59% (19.7 times higher than CornerSense), leading to a precision of 57% and F1-score of 66%. These substantially higher FPRs and consequently lower precision and F1-scores can be attributed to the baseline's direct implementation of [21] without effectively compensating the signal variations caused by the robot's movement and hardware-induced phase offset.

4.3 Computational Complexity and Real-time Analysis

We now analyze the computational complexity of the key components within the CornerSense one by one, given N CSI measurements each with K subcarriers:

Reference Path Extraction: The initial step involves applying PCA to extract the components of the reference path. This necessitates computing the covariance matrix with a computational complexity of $O(K^2N)$. Additionally, calculating eigenvalues and eigenvectors has a complexity of $O(K^3)$, essential for determining the principal components.

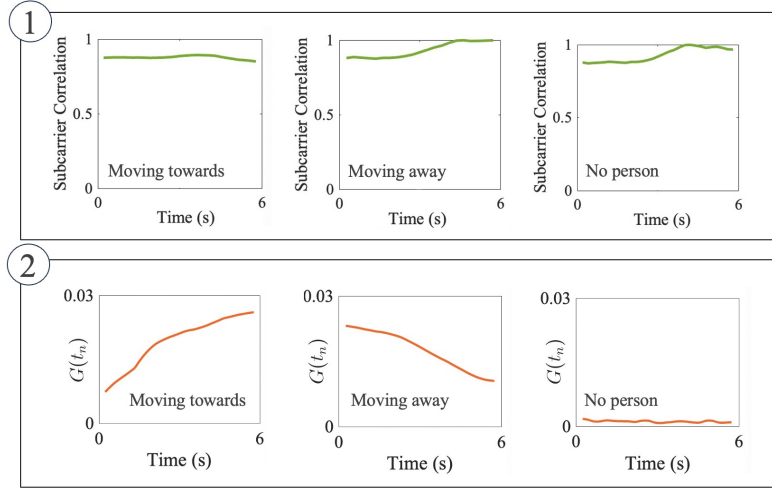


Fig. 13. Comparison of metric variations between baseline [21] and our CornerSense.

Table 3. Performance of the baseline [21].

		Corridor	Staircase	Room	Average
Proximity detection	TPR	0.88	0.80	0.85	0.84
	FPR	0.45	0.53	0.40	0.46
	Precision	0.49	0.43	0.52	0.48
	F1-score	0.63	0.56	0.64	0.61
Region classification	TPR	0.80	0.78	0.75	0.78
	FPR	0.53	0.60	0.63	0.59
	Precision	0.60	0.57	0.54	0.57
	F1-score	0.69	0.66	0.63	0.66

RMPOC Algorithm (Alg. 1): The RMPOC algorithm involves the process of extracting the dominant human-reflected path using another round of PCA, incurring a complexity of $O(K^2N + K^3)$. Moreover, calculating the AoA using the MUSIC algorithm [25] for robot motion removal typically incurs a computational complexity of $O(N^3)$. Finally, the phase offset compensation introduces additional complexity of $O(N)$.

Subcarrier Phase Difference: The subcarrier phase difference metric calculation is performed for each sample, resulting in a complexity of $O(KN)$.

When multiple antennas are used to collect multiple streams of CSI data at the same time, all the above complexities terms should be multiplied by the number of streams.

In practice, for 1000 CSI measurements, CSI collection takes around 1s (using 1kHz sampling rate) and CSI extraction from the traces takes 0.400~0.500s. The subsequent processing includes three parts: components extraction for the reference path and dominant human-reflected path (0.010~0.100s), RMPOC algorithm (0.010~0.100s), and proximity detection (0.003~0.050s), all running on a computer powered by an Intel i7 processor using MATLAB. In total, it takes less than 1.70 s to generate instructions for the robot to stop or continue moving. During this processing time, with the robot moving at 0.2 m/s in our setting (falls within the typical safe indoor robot speed range of 0.1-0.25 m/s [13]), it would only travel 0.34m, which effectively prevents any collision between the robot and targets around the corner. Notably, the robot can begin collecting CSI measurements while moving, well before reaching the critical decision point. We further remark that the algorithm's execution time could

Table 4. TPR and FPR of CornerSense when processing using different number of CSI measurements N .

# of CSI measurements		400	600	800	1000	1200	1400
Proximity detection	TPR	0.54	0.68	0.72	0.89	0.93	0.96
	FPR	0.19	0.15	0.12	0.06	0.04	0.03
Region classification	TPR	0.64	0.75	0.83	0.87	0.91	0.95
	FPR	0.18	0.14	0.10	0.07	0.05	0.03

Table 5. TPR and FPR of CornerSense under different target and robot speeds.

(a) Three target speeds.			(b) Three robot speeds.		
Target	TPR	FPR	Robot	TPR	FPR
1 ~ 2 m/s	5/5	0/5	0.5 m/s	5/5	1/5
0.4 ~ 0.8 m/s	5/5	0/5	0.2 m/s	5/5	0/5
0.1 ~ 0.3 m/s	5/5	0/5	0.1 m/s	5/5	0/5

be further reduced by implementing it in C/C++ and accelerating it with advanced hardware such as FPGAs or GPUs.

5 DISCUSSION AND LIMITATIONS

Impact of Robot and Target Speeds: The speed of the target or robot does not fundamentally affect the algorithms used in CornerSense, nor does it alter the characteristics of the subcarrier phase difference metric. We conducted experiments at various target and robot speeds, and the results, presented in Table 5, support this observation. Moreover, since the robot collects CSI within a predefined region, extremely high speeds may lead to an insufficient number of CSI measurements being captured. To investigate this, we conducted additional tests varying the number of collected CSI packets (i.e., N) with the results summarized in Table 4. These results indicate that when $N < 1000$, corresponding to robot speeds exceeding 2 m/s and data collection durations under 1 second, the TPR for both proximity detection and region classification drops by at least 7% and 8%, respectively. Nevertheless, due to safety considerations, indoor robot speeds are typically constrained. In fact, based on our observations, speeds greater than 0.8 m/s already pose safety risks and exceed the typical operational limits for indoor use. Therefore, the reduced algorithm performance under such high-speed conditions is not a practical concern in real-world deployments. We remark that the real-time velocity data can directly obtained from standard onboard sensors like IMU.

It should be noted that our system requires robot velocity as an input parameter for calculations. In our experiments, while we used preset uniform velocity values, the actual robot motion involved acceleration from rest and slight velocity variations. Despite this discrepancy between assumed uniform velocity and actual varying velocity being one source of error, our system maintained a TPR above 94%. Future implementations could potentially achieve even higher accuracy by incorporating real-time robot velocity data corresponding to each CSI sample timestamp, rather than using preset uniform values.

Impact of Multiple Targets: In its current form, CornerSense is designed with the objective of detecting the proximity of a single target around a corner. However, it is of interest to explore whether CornerSense can extend its proximity detection capabilities to multi-person corner scenarios. We have thoroughly investigated three distinct cases while acknowledging practical limitations:

Case 1: Two moving people on the other side of the corner. To evaluate the capability of detecting moving multiple targets, we conducted simple experiments in a two-target setting, covering three representative cases:

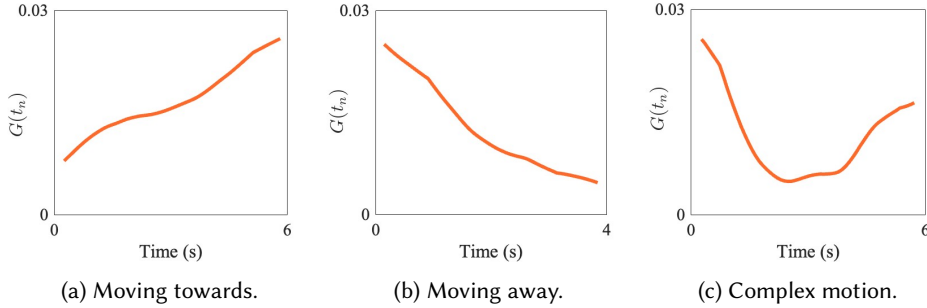


Fig. 14. Subcarrier phase difference trends when using CornerSense to detect two moving targets.

(1) both individuals moving toward the corner side by side, (2) both moving away from the corner side by side, and (3) one individual moving toward the corner while the other moves away. The results, presented in Figure 14, show that CornerSense correctly identifies the first two scenarios, as expected. In the third scenario, CornerSense reflects the motion state of the target closest to the robot. Initially, the closer individual is the one moving away, resulting in a decrease in subcarrier phase difference. As the individuals pass each other and the approaching individual becomes closer to the robot, the subcarrier phase difference begins to increase. This behavior demonstrates that CornerSense effectively captures and responds to dynamic changes in target proximity, even in mixed-motion scenarios. Overall, these results highlight CornerSense’s potential to handle multiple targets. However, a systematic design and comprehensive evaluation for such multi-target scenarios are beyond the scope of this work and are left for future investigation.

Case 2: Three or more targets on the other side of the corner. This represents a complex scenario where, given typical corner widths, both the reference path and dominant human-reflected path are blocked. In such cases, our system detects the absence of these two important path components in the PCA results, indicating that the corner area is crowded with multiple people or obstructed. This detection capability allows the robot to appropriately reduce its speed to prevent potential collisions. For readers interested in determining the movement direction of multiple targets in such blocked scenarios, we note that when both Tx and Rx are mounted on the robot, the system can avoid signal blockage and maintain its functionality. A detailed analysis of this configuration is provided in Appendix 5.

Case 3: Multiple stationary people near the corner with a moving target on the other side of the corner. As demonstrated in our third group of experiments (Section 4), CornerSense maintains its high performance even in scenarios where multiple people are sitting or standing around the corner. This indicates that the presence of static multiple targets has minimal impact on our system’s effectiveness.

Moreover, when multiple people are simultaneously walking on the other side of the corner with sufficiently wide corners that are not blocked by multiple targets, given the current limitations of WiFi bandwidth, it is indeed challenging to distinguish and capture the path passing through each person and separately determine the proximity status of each target. We plan to explore this aspect in our future work to make the robot’s motion sensing more robust and intelligent.

Impact of Center Frequency and Bandwidth: The center frequency has minimal impact on CornerSense’s performance. In contrast, increased bandwidth, providing a higher density of subcarriers, can significantly enhance detection accuracy. Specifically, a denser subcarrier distribution enables more effective dimensionality reduction during reference path extraction. Moreover, higher subcarrier density allows for more accurate extraction of the dominant human-reflected path, enabling finer detection of path length variations caused by human motion. This, in turn, leads to improved proximity detection accuracy. While CornerSense currently operates

under conventional WiFi sensing settings (center frequency of 5.32 GHz with 20 MHz bandwidth), its architecture is inherently compatible with future wideband systems, requiring no algorithmic modifications for deployment.

Extended Capabilities and Applications: It is worth noting that CornerSense is developed under the context of integrated sensing and communications (ISAC), where the robot communicates with a fixed AP while performing sensing. Some readers might wonder whether CornerSense could work in a more autonomous scenario where both Tx and Rx are carried by the mobile robot (without requiring a fixed AP). We have theoretically and experimentally verified that CornerSense remains effective when both the Tx and Rx are on the robot, with detailed discussion provided in Appendix 5.

Furthermore, CornerSense effectively detects target moving towards, moving away, and no-target situations without prior knowledge of corner width or Tx location. Some readers may be interested in whether CornerSense can further estimate the distance between the target and the robot. We propose two different approaches to achieve this capability, with detailed analysis provided in Appendix 6.

While our work focuses on the classic corner scenario, it may be valuable to consider the implications of robot mobility on target motion sensing in other NLoS or LoS environments. To this end, we extend our discussion to include an analysis of indoor NLoS and outdoor scenarios in Appendix 7, where we explore the unique challenges and considerations for these different contexts.

6 RELATED WORK

Our work intersects four key research domains: wireless sensing for human proximity/activity, traditional sensing for mobile robots, wireless sensing on mobile robots, and passive proximity detection for NLoS scenarios. We review relevant work in each area and highlight the limitations that CornerSense addresses.

Wireless Sensing for Proximity and Activity Detection Wireless signals, primarily CSI and millimeter-wave (mmWave) radar, have been extensively explored for detecting human presence, proximity, and activity. WiFi-based systems leverage signal variations caused by human movement for applications like fall detection (e.g., WiFall [44]), through-wall sensing (e.g., WiVi [54]), gesture recognition [2], and fine-grained activity monitoring [35]. These systems typically achieve high accuracy but rely crucially on stationary transceivers. mmWave radar offers higher spatial resolution and sensitivity to subtle movements, enabling tasks like vital sign monitoring [5], gait analysis [27], and even attempts at NLoS detection [26]. However, mmWave's inherent high directionality and narrow beamwidth make it highly susceptible to blockage and poorly suited for robust, wide-angle detection around corners, especially when the sensing platform itself is moving. Beamforming requirements and limited field-of-view further complicate its use in the dynamic, unstructured NLoS scenarios encountered by mobile robots. While both WiFi and mmWave show promise for proximity detection, existing approaches are fundamentally designed for and limited to stationary setups.

Traditional Sensing for Mobile Robots Mobile robots predominantly rely on LoS sensors for navigation and obstacle avoidance. LiDAR provides precise geometric mapping and localization (e.g., in SLAM systems [16]) but is ineffective around corners or through obstacles. Vision-based systems (cameras) enable rich scene understanding and object detection [36] but fail in low-light conditions, suffer from privacy concerns, and are fundamentally LoS-limited. Ultrasonic sensors offer low-cost proximity detection but have limited range and accuracy. Inertial Measurement Units (IMUs) and wheel odometry track robot movement but accumulate drift over time. These core robotic sensors excel in LoS perception but are fundamentally incapable of detecting objects or humans hidden around corners (NLoS), creating significant blind spots critical for safety and navigation in human environments.

Wireless Sensing on Mobile Robots Recent work explores leveraging the robot's onboard WiFi interface beyond communication. Arun et al. [6] integrated WiFi sensing with odometry in a GraphSLAM framework

(P2SLAM), significantly improving localization accuracy over pure odometry. Ayyalasomayajula et al. developed LocAP [7] for precise mapping of wireless infrastructure and DLoc [8] for deep learning-based device localization, simplifying WiFi-based positioning tasks. Jadhav et al. [23] demonstrated accurate Angle-of-Arrival (AoA) estimation for robot-to-robot interaction in complex environments. These works represent significant advances in active WiFi sensing for mobile robots, focusing on tasks like SLAM, infrastructure/device localization, and relative positioning of cooperative wireless devices. While demonstrating the utility of mobile WiFi sensing, these approaches do not address the challenge of passive, device-free detection of non-cooperative human targets, particularly in NLoS scenarios. The weak, noise-prone signal reflections from humans are fundamentally different and more challenging to isolate than signals from active devices or infrastructure, especially amidst robot motion.

Passive Proximity Detection for NLoS Scenarios Detecting passive targets without attached devices around corners is an active research area. Radar-based techniques are prominent: CornerRadar [50] uses specialized radar hardware and CNNs for high-accuracy NLoS detection, but requires stationary transceivers. Hu et al. [22] explored antenna movement direction detection but explicitly cannot detect human proximity during receiver movement. Acoustic methods exploit sound reflections for NLoS perception [53] but face challenges with ambient noise and limited range. Some WiFi-based approaches with stationary setups attempt NLoS inference [30, 58], but rely on static environmental assumptions. Existing passive NLoS detection methods are overwhelmingly designed for stationary sensors. Techniques attempting to handle transceiver movement either focus on different problems (e.g., antenna motion characterization) or lack the robustness required for continuous proximity detection during robot motion. Enabling reliable, device-free human proximity detection around corners while the sensing platform (robot) is moving remains an unsolved challenge.

Positioning of CornerSense The review above reveals a clear gap. While progress exists in wireless sensing (largely stationary), robotic perception (LoS-limited), mobile robot WiFi (active sensing), and passive NLoS detection (static platforms), no prior work enables robust, passive, device-free detection of human proximity around corners using WiFi sensing on a continuously moving mobile robot. CornerSense directly addresses this gap. Unlike active localization systems on robots (e.g., [6, 23]), CornerSense tackles the fundamentally different challenge of extracting weak, passive human reflections from noisy CSI dominated by the robot’s own motion. Unlike stationary NLoS detection (e.g., [50]), CornerSense is designed specifically for the dynamic scenario where both the sensor (robot) and the target (human) may be moving. Our novel virtual path-augmented, two-stage dominant path extraction approach is the key innovation that disentangles these complex signal interactions, enabling reliable NLoS proximity detection where traditional sensors fail and prior wireless approaches are insufficient.

7 CONCLUSION

In this paper, we introduced CornerSense, a new WiFi sensing framework designed to enable mobile robots to achieve human proximity detection at corners by effectively compensating the robot’s motion and the hardware-induced phase offset in the extracted dominant human-reflected path. At the core of CornerSense is the virtual path-augmented two-stage PCA approach, which effectively extracts both the reference path and the dominant human-reflected path. Through the formation of aug-CSI power and our proposed RMPOC algorithm, CornerSense successfully addresses key challenges in mobile WiFi sensing: extracting individual paths under limited bandwidth, compensating for hardware-induced phase offset, and achieving reliable proximity detection on mobile robots. In nine distinct corner scenarios in three groups and four different walking patterns, CornerSense achieved a TPR of 96% in detecting proximity at corners. Furthermore, CornerSense enables region classification of the target on the other side of the corner, achieving a TPR of 95% in region classification. The FPRs of proximity detection and region classification are nearly 15.3 times and approximately 19.7 times lower, respectively, than those achieved

by directly applying the latest proximity detection algorithm developed for stationary WiFi transceivers. These results demonstrate the potential of mobile WiFi sensing as a promising complement to mobile robotic sensors for non-line-of-sight human detection. Future work will focus on extending the design principles of CornerSense to more general scenarios beyond corner-specific settings, as well as to multi-target sensing environments. These extensions will require the development of additional techniques to address the increased multipath complexity in such settings.

Acknowledgments

The work of He Chen is supported in part by RGC Early Career Scheme (ECS) under Project 24210524, the CUHK Strategic Seed Funding for Collaborative Research Scheme under Project 3136053 and the CUHK Direct Grant for Research under Project 4055229.

The research work described in this paper was conducted in the JC STEM Lab of Advanced Wireless Networks for Mission-Critical Automation and Intelligence funded by The Hong Kong Jockey Club Charities Trust.

References

- [1] 2024. *Wireless InSite® 3D Wireless Propagation Software*. <https://www.remcom.com/wireless-insite-propagation-software> Accessed: 2024-03-14.
- [2] Heba Abdelnasser, Moustafa Youssef, and Khaled A Harras. 2015. Wigest: A ubiquitous wifi-based gesture recognition system. In *2015 IEEE conference on computer communications (INFOCOM)*. IEEE, 1472–1480.
- [3] Fadel Adib and Dina Katabi. 2013. See through walls with WiFi!. In *Proceedings of the ACM SIGCOMM 2013 conference on SIGCOMM*. 75–86.
- [4] AgileX Robotics Ltd. 2020. SCOUT Mini. <https://www.agilex.ai/chassis/11>. Accessed: 2020-07-24.
- [5] Adeel Ahmad, June Chul Roh, Dan Wang, and Aish Dubey. 2018. Vital signs monitoring of multiple people using a FMCW millimeter-wave sensor. In *2018 IEEE Radar Conference (RadarConf18)*. IEEE, 1450–1455.
- [6] Aditya Arun, Roshan Ayyalasomayajula, William Hunter, and Dinesh Bharadia. 2022. P2slam: Bearing based wifi slam for indoor robots. *IEEE Robotics and Automation Letters* 7, 2 (2022), 3326–3333.
- [7] Roshan Ayyalasomayajula, Aditya Arun, Chenfeng Wu, Anees Shaikh, Shrivatsan Rajagopalan, Yige Hu, Shreya Ganesaraman, Christopher J Rossbach, Aravind Seetharaman, Emmett Witchel, et al. 2020. {LocAP}: Autonomous millimeter accurate mapping of {WiFi} infrastructure. In *17th USENIX Symposium on Networked Systems Design and Implementation (NSDI 20)*. 1115–1129.
- [8] Roshan Ayyalasomayajula, Aditya Arun, Chenfeng Wu, Sanatan Sharma, Abhishek Rajkumar Sethi, Deepak Vasisht, and Dinesh Bharadia. 2020. Deep learning based wireless localization for indoor navigation. In *Proceedings of the 26th Annual International Conference on Mobile Computing and Networking*. 1–14.
- [9] David Brewster. 1815. IX. On the laws which regulate the polarisation of light by reflexion from transparent bodies. By David Brewster, LL. DFRS Edin. and FSA Edin. In a letter addressed to Right Hon. Sir Joseph Banks, Bart. KBPR S. *Philosophical Transactions of the Royal Society of London* 105 (1815), 125–159.
- [10] Zhaoxin Chang, Fusang Zhang, Jie Xiong, Weiyang Chen, and Daqing Zhang. 2024. MSense: Boosting Wireless Sensing Capability Under Motion Interference. In *The 30th Annual International Conference on Mobile Computing and Networking (ACM MobiCom'24)*.
- [11] Lili Chen, Xiaojiang Chen, Ligang Ni, Yao Peng, and Dingyi Fang. 2017. Human behavior recognition using Wi-Fi CSI: Challenges and opportunities. *IEEE Communications Magazine* 55, 10 (2017), 112–117.
- [12] Zhenghua Chen, Le Zhang, Chaoyang Jiang, Zhiguang Cao, and Wei Cui. 2018. WiFi CSI based passive human activity recognition using attention based BLSTM. *IEEE Transactions on Mobile Computing* 18, 11 (2018), 2714–2724.
- [13] Iong Chio, Kaicheng Ruan, Zehao Wu, Kit Long Wong, Lap Mou Tam, and Qingsong Xu. 2022. Design and autonomous navigation of a new indoor disinfection robot based on disinfection modeling. *IEEE transactions on automation science and engineering* 20, 1 (2022), 649–661.
- [14] Neena Damodaran, Elis Haruni, Muyassar Kokhkarova, and Jörg Schäfer. 2020. Device free human activity and fall recognition using WiFi channel state information (CSI). *CCF Transactions on Pervasive Computing and Interaction* 2 (2020), 1–17.
- [15] Sharifah Mastura Syed Mohd Daud, Mohd Yusmialil Putera Mohd Yusof, Chong Chin Heo, Lay See Khoo, Mansharan Kaur Chainchel Singh, Mohd Shah Mahmood, and Hapizah Nawawi. 2022. Applications of drone in disaster management: A scoping review. *Science & Justice* 62, 1 (2022), 30–42.
- [16] César Debeunne and Damien Vivet. 2020. A review of visual-LiDAR fusion based simultaneous localization and mapping. *Sensors* 20, 7 (2020), 2068.
- [17] Albert Einstein et al. 1905. On the electrodynamics of moving bodies. *Annalen der physik* 17, 10 (1905), 891–921.

- [18] Shiwei Fang, Ron Alterovitz, and Shahriar Nirjon. 2019. Non-line-of-sight around the corner human presence detection using commodity WiFi devices. In *Proceedings of the 1st ACM International Workshop on Device-Free Human Sensing*. 22–26.
- [19] Daniel Halperin, Wenjun Hu, Anmol Sheth, and David Wetherall. 2011. Tool release: Gathering 802.11 n traces with channel state information. *ACM SIGCOMM computer communication review* 41, 1 (2011), 53–53.
- [20] Wenbin Hou, Zhihua Xiong, Changsheng Wang, and Howard Chen. 2022. Enhanced ant colony algorithm with communication mechanism for mobile robot path planning. *Robotics and Autonomous Systems* 148 (2022), 103949.
- [21] Yuqian Hu, Muhammed Zahid Ozturk, Beibei Wang, Chenshu Wu, Feng Zhang, and KJ Ray Liu. 2022. Robust Passive Proximity Detection using Wi-Fi. *IEEE Internet of Things Journal* (2022).
- [22] Yuqian Hu, M Zahid Ozturk, Feng Zhang, Beibei Wang, and KJ Ray Liu. 2021. Robust device-free proximity detection using wifi. In *ICASSP 2021-2021 IEEE International Conference on Acoustics, Speech and Signal Processing (ICASSP)*. IEEE, 7918–7922.
- [23] Ninad Jadhav, Weiyang Wang, Diana Zhang, Oussama Khatib, Swaran Kumar, and Stephanie Gil. 2022. A wireless signal-based sensing framework for robotics. *The International Journal of Robotics Research* 41, 11-12 (2022), 955–992.
- [24] Ameer Tamoor Khan, Shuai Li, and Xinwei Cao. 2022. Human guided cooperative robotic agents in smart home using beetle antennae search. *Science China Information Sciences* 65, 2 (2022), 122204.
- [25] Manikanta Kotaru, Kiran Joshi, Dinesh Bharadia, and Sachin Katti. 2015. Spotfi: Decimeter level localization using wifi. In *Proceedings of the 2015 ACM Conference on Special Interest Group on Data Communication*. 269–282.
- [26] Gen Li, Yun Ge, Yiyu Wang, Qingwu Chen, and Gang Wang. 2022. Detection of human breathing in non-line-of-sight region by using mmWave FMCW radar. *IEEE Transactions on Instrumentation and Measurement* 71 (2022), 1–11.
- [27] Jincheng Li, Binbin Li, Lin Wang, and Wenyuan Liu. 2023. Passive multiuser gait identification through micro-Doppler calibration using mmWave radar. *IEEE Internet of Things Journal* 11, 4 (2023), 6868–6877.
- [28] Kerui Li, Zhipeng Li, Ze Xiong, Yingxi Wang, Haitao Yang, Wenxin Xu, Lin Jing, Meng Ding, Jian Zhu, John S Ho, et al. 2022. Thermal camouflaging MXene robotic skin with bio-inspired stimulus sensation and wireless communication. *Advanced Functional Materials* 32, 23 (2022), 2110534.
- [29] Wenda Li, Bo Tan, and Robert J Piechocki. 2018. Wifi-based passive sensing system for human presence and activity event classification. *IET Wireless Sensor Systems* 8, 6 (2018), 276–283.
- [30] Xiaohui Li, Xiong Cai, Yongqiang Hei, and Ruiyang Yuan. 2017. NLOS identification and mitigation based on channel state information for indoor WiFi localisation. *Iet Communications* 11, 4 (2017), 531–537.
- [31] Evangelos Liatsikos, Arman Tsaturyan, Iason Kyriazis, Panagiotis Kallidonis, Dimitris Manolopoulos, and Anastasios Magoutas. 2022. Market potentials of robotic systems in medical science: analysis of the Avatera robotic system. *World Journal of Urology* 40, 1 (2022), 283–289.
- [32] Yongsen Ma, Gang Zhou, and Shuangquan Wang. 2019. WiFi sensing with channel state information: A survey. *ACM Computing Surveys (CSUR)* 52, 3 (2019), 1–36.
- [33] Andrzej Maćkiewicz and Waldemar Ratajczak. 1993. Principal components analysis (PCA). *Computers & Geosciences* 19, 3 (1993), 303–342.
- [34] Francesca Meneghelli, Domenico Garlisi, Nicolò Dal Fabbro, Ilaria Tinnirello, and Michele Rossi. 2022. Sharp: Environment and person independent activity recognition with commodity ieee 802.11 access points. *IEEE Transactions on Mobile Computing* (2022).
- [35] Majid Ghosian Moghaddam, Ali Asghar Nazari Shirehjini, and Shervin Shirmohammadi. 2023. A WiFi-based method for recognizing fine-grained multiple-subject human activities. *IEEE Transactions on Instrumentation and Measurement* 72 (2023), 1–13.
- [36] Khan Muhammad, Tanveer Hussain, Hayat Ullah, Javier Del Ser, Mahdi Rezaei, Neeraj Kumar, Mohammad Hijji, Paolo Bellavista, and Victor Hugo C De Albuquerque. 2022. Vision-based semantic segmentation in scene understanding for autonomous driving: Recent achievements, challenges, and outlooks. *IEEE Transactions on Intelligent Transportation Systems* 23, 12 (2022), 22694–22715.
- [37] Riku Murai, Joseph Ortiz, Sajad Saeedi, Paul HJ Kelly, and Andrew J Davison. 2023. A robot web for distributed many-device localisation. *IEEE Transactions on Robotics* (2023).
- [38] Kai Niu, Xuanzhi Wang, Fusang Zhang, Rong Zheng, Zhiyun Yao, and Daqing Zhang. 2022. Rethinking Doppler effect for accurate velocity estimation with commodity WiFi devices. *IEEE Journal on Selected Areas in Communications* 40, 7 (2022), 2164–2178.
- [39] Laetitia Thirion-Lefevre and Régis Guinvarc'h. 2018. The double Brewster angle effect. *Comptes Rendus. Physique* 19, 1-2 (2018), 43–53.
- [40] Raghav H Venkatnarayanan and Muhammad Shahzad. 2019. Enhancing indoor inertial odometry with wifi. *Proceedings of the ACM on Interactive, Mobile, Wearable and Ubiquitous Technologies* 3, 2 (2019), 1–27.
- [41] Wei Wang, Alex X Liu, and Muhammad Shahzad. 2016. Gait recognition using wifi signals. In *Proceedings of the 2016 ACM International Joint Conference on Pervasive and Ubiquitous Computing*. 363–373.
- [42] Wei Wang, Alex X Liu, Muhammad Shahzad, Kang Ling, and Sanglu Lu. 2015. Understanding and modeling of wifi signal based human activity recognition. In *Proceedings of the 21st annual international conference on mobile computing and networking*. 65–76.
- [43] Wei Wang, Alex X Liu, Muhammad Shahzad, Kang Ling, and Sanglu Lu. 2017. Device-free human activity recognition using commercial WiFi devices. *IEEE Journal on Selected Areas in Communications* 35, 5 (2017), 1118–1131.

- [44] Yuxi Wang, Kaishun Wu, and Lionel M Ni. 2016. Wifall: Device-free fall detection by wireless networks. *IEEE Transactions on Mobile Computing* 16, 2 (2016), 581–594.
- [45] Zhu Wang, Bin Guo, Zhiwen Yu, and Xingshe Zhou. 2018. Wi-Fi CSI-based behavior recognition: From signals and actions to activities. *IEEE Communications Magazine* 56, 5 (2018), 109–115.
- [46] Yuan Wu, Ruizhi Chen, Wei Li, Yue Yu, Haitao Zhou, and Ke Yan. 2021. Indoor positioning based on walking-surveyed Wi-Fi fingerprint and corner reference trajectory-geomagnetic database. *IEEE sensors journal* 21, 17 (2021), 18964–18977.
- [47] Tong Xin, Bin Guo, Zhu Wang, Pei Wang, Jacqueline Chi Kei Lam, Victor Li, and Zhiwen Yu. 2018. FreeSense: A robust approach for indoor human detection using Wi-Fi signals. *Proceedings of the ACM on Interactive, Mobile, Wearable and Ubiquitous Technologies* 2, 3 (2018), 1–23.
- [48] Yang Xu, Wei Yang, Jianxin Wang, Xing Zhou, Hong Li, and Liusheng Huang. 2018. WiStep: Device-free step counting with WiFi signals. *Proceedings of the ACM on Interactive, Mobile, Wearable and Ubiquitous Technologies* 1, 4 (2018), 1–23.
- [49] Huan Yan, Yong Zhang, Yujie Wang, and Kangle Xu. 2019. WiAct: A passive WiFi-based human activity recognition system. *IEEE Sensors Journal* 20, 1 (2019), 296–305.
- [50] Shichao Yue, Hao He, Peng Cao, Kaiwen Zha, Masayuki Koizumi, and Dina Katabi. 2022. Cornerradar: Rf-based indoor localization around corners. *Proceedings of the ACM on Interactive, Mobile, Wearable and Ubiquitous Technologies* 6, 1 (2022), 1–24.
- [51] Bin-Bin Zhang, Dongheng Zhang, Ruiyuan Song, Binquan Wang, Yang Hu, and Yan Chen. 2023. *RF-Search: Searching Unconscious Victim in Smoke Scenes with RF-enabled Drone*. Association for Computing Machinery, New York, NY, USA. <https://doi.org/10.1145/3570361.3613305>
- [52] Fusang Zhang, Jie Xiong, Zhaoxin Chang, Junqi Ma, and Daqing Zhang. 2022. Mobi2Sense: empowering wireless sensing with mobility. In *Proceedings of the 28th Annual International Conference on Mobile Computing And Networking*. 268–281.
- [53] Lei Zhang, Danjie Huang, Xinheng Wang, Christian Schindelhauer, and Zhi Wang. 2017. Acoustic NLOS identification using acoustic channel characteristics for smartphone indoor localization. *Sensors* 17, 4 (2017), 727.
- [54] Lei Zhang, Xin Ruan, and Ju Wang. 2019. WiVi: A ubiquitous violence detection system with commercial WiFi devices. *IEEE Access* 8 (2019), 6662–6672.
- [55] Lei Zhang, Cong Wang, Maode Ma, and Daqing Zhang. 2019. WiDGR: Direction-independent gait recognition system using commercial Wi-Fi devices. *IEEE Internet of Things Journal* 7, 2 (2019), 1178–1191.
- [56] Lei Zhang, Cong Wang, and Daqing Zhang. 2021. Wi-PIGR: Path independent gait recognition with commodity Wi-Fi. *IEEE Transactions on Mobile Computing* 21, 9 (2021), 3414–3427.
- [57] Rui Zhou, Xiang Lu, Pengbiao Zhao, and Jiesong Chen. 2017. Device-free presence detection and localization with SVM and CSI fingerprinting. *IEEE Sensors Journal* 17, 23 (2017), 7990–7999.
- [58] Zimu Zhou, Zheng Yang, Chenshu Wu, Longfei Shangguan, Haibin Cai, Yunhao Liu, and Lionel M Ni. 2015. WiFi-based indoor line-of-sight identification. *IEEE Transactions on Wireless Communications* 14, 11 (2015), 6125–6136.

APPENDIX

Appendix 1: A Brief Primer on PCA

PCA is a widely used technique for dimensionality reduction and feature extraction, categorized as an unsupervised learning method. PCA projects the original data onto a lower-dimensional space through a linear transformation, maximizing the variance captured by the new dimensions while minimizing the correlation between them. The resulting dimensions, called principal components, represent the most significant features of the original data. Applying PCA along f_m reduces CSI dimensionality while preserving significant features. To better understand how PCA facilitates our phase analysis, we establish two key properties [33] that will be referenced in subsequent sections:

Property 1: Consider a dataset generated by the linear combination:

$$X(f_m, t_n) = \sum_{i=1}^K C_i x_i(f_m, t_n), \quad m = 1, \dots, M, n = 1, \dots, N, \quad (24)$$

where C_i are constant coefficients, and $x_i(f_m, t_n)$ represents the component measured at frequency f_m and time instance t_n . Specifically, t_n indicates different sampling times, and f_m represents different frequency points at which the measurements are taken. Each $x_i(f_m, t_n)$ is a function of frequency and may vary with time. If there exists a strong hierarchy among the coefficients, i.e., $C_1 \gg C_2 \gg \dots \gg C_K$, the linear combinations of $C_1 x_1(f_m, t_n)$ across different frequencies f_m manifest as the leading principal component in the output of PCA.

Property 2: For signal components composed of two uncorrelated parts:

$$X(f_m, t_n) = g(f_m, t_n) + h(f_m, t_n), \quad \text{with } \mathbb{E}[(g - \mathbb{E}[g])(h - \mathbb{E}[h])] \approx 0, \quad (25)$$

where $X(f_m, t_n)$ represents the signal measured at frequency f_m and time instance t_n . This signal is composed of two components: $g(f_m, t_n)$ and $h(f_m, t_n)$, both of which are functions of frequency and time. Across consecutive time samples, these components are linearly uncorrelated, as indicated by their cross-correlation being approximately zero ($\mathbb{E}[(g - \mathbb{E}[g])(h - \mathbb{E}[h])] \approx 0$, where $\mathbb{E}[\cdot]$ denotes the expectation operator). When g and h have comparable variances (i.e., $\mathbb{E}[(g - \mathbb{E}[g])^2] \approx \mathbb{E}[(h - \mathbb{E}[h])^2]$), PCA will resolve these uncorrelated subcomponents into distinct principal components, even when their magnitudes are similar. This property enables us to separate different signal components effectively, provided they exhibit distinct statistical characteristics.

These properties form the theoretical foundation for our subsequent analysis, where we will leverage PCA to isolate and analyze specific components of interest in our data.

Appendix 2: Analysis of Two Dominant Paths

In $\Omega_1(t_n)$, the reference path (shown as the purple dotted line in Figure 15) undergoes a single wall reflection and represents the strongest signal path. While geometrically possible, a double-wall reflected path (shown as the purple dashed line) is typically either non-existent or negligible in most scenarios. Other dynamic paths involving multiple reflections are significantly weaker and can be disregarded, as illustrated in Figure 15. The negligible impact of the double-wall reflected path can be attributed to two factors. First, in most corner scenarios, such as T-corners or when the Tx is located far away from the corner, this path does not exist geometrically. Second, even in corner scenarios where such a path is geometrically feasible, the Brewster angle effect [9] leads to its effective suppression. Specifically, as illustrated by the purple dashed line in Figure 15, the incident angle θ_{in} of the first reflection in the double-wall path substantially exceeds the Brewster angle. Given that the Brewster angle for air-to-wall transmission is approximately 60 degrees [9, 39], signals with incident angles beyond this threshold experience near-complete suppression of the reflected component, effectively eliminating the contribution of this path.

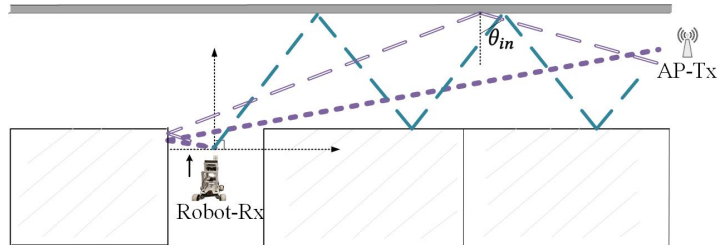


Fig. 15. Representative paths in $\Omega_1(t_n)$. Here, the purple dotted line representing the reference path, which undergoes only a single wall reflection, is the strongest path. The dashed lines represent the paths experiencing at least double wall reflections.

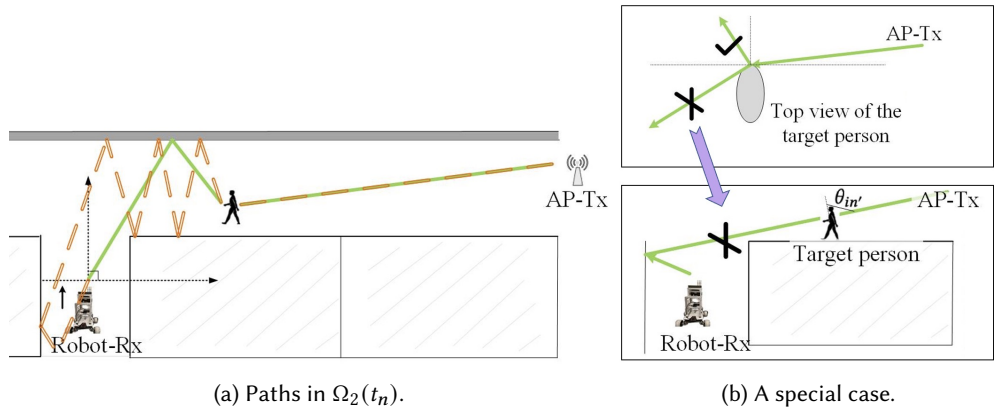


Fig. 16. (a) Representative paths in $\Omega_2(t_n)$, in which the green solid line represents the path with minimal reflection attenuation. (b) When signals interact with the human body, we can disregard paths with severe body penetration (marked with a cross). Additionally, considering the Brewster angle effect, there will be no structurally similar single reflection path through the human body resembling the reference path (the purple solid dashed line) shown in Figure 15. Therefore, Ω_2 contains no paths similar to the reference path in $\Omega_1(t_n)$, leaving only the green solid path in (a) as the dominant human-reflected path.

Similarly, in $\Omega_2(t_n)$, there exists a dominant path that travels from the Tx to the human target and then to Rx on the robot, denoted as $H_u(f, t_n)$. This path, termed the dominant human-reflected path, experiences only a single reflection off the wall and is illustrated by the green path in Figure 16a. While the corner geometry might suggest the possibility of multiple dominant human-reflected paths, physical constraints limit us to only one such path in $\Omega_2(t_n)$. This uniqueness can be explained by two key physical phenomena: 1) As illustrated in Figure 16b, signals cannot effectively penetrate through the human body after wall reflection, substantially suppressing potential paths that would require body penetration. 2) The Brewster angle effect further constrains possible paths, as reflections effectively disappear when the incident angle $\theta_{in'}$ from air to human body exceeds 53 degrees [39]. This physical limitation rules out paths marked with a cross in Figure 16b, including those that might otherwise mirror the reference path shown in Figure 15. Consequently, the only feasible dominant human-reflected path in $\Omega_2(t_n)$ is the one shown by the green solid line in Figure 16(a). Other paths in $\Omega_2(t_n)$ involving multiple reflections are substantially weaker and can be disregarded, as indicated in Figure 16a.

Table 6. The Percentage of Different AoA Numbers Across Three Corner Scenarios.

Number of AoAs	0	1	2	3	4	[5,∞)
The staircase corner	0.22%	0.94%	98.24%	0.45%	0.11%	0.04%
The corridor corner	0.14%	0.77%	98.10%	0.67%	0.23%	0.09%
The room-entrance corner	0.19%	0.91%	97.78%	0.63%	0.33%	0.16%

Based on the preceding analysis of path characteristics in $\Omega_1(t_n)$ and $\Omega_2(t_n)$, we can deduce that the CSI in corner scenarios primarily consists of two dominant paths: the reference path $H_r(f, t_n)$ and the dominant human-reflected path $H_u(f, t_n)$, while other paths are significantly weaker in comparison. To validate this conjecture, we conduct experiments across three different corner scenarios. As shown in Tab. 6, when calculating the AoAs of detected paths using the method in [25], we observe that the number of stable AoAs in corner scenarios is predominantly two, with merely around 1% of samples showing more than two AoAs. This empirical evidence confirms our conjecture that besides the reference path, there is indeed only one dominant human-reflected path in corner scenarios. It is worth noting that this two-path dominance holds true when using omnidirectional antennas, which can transmit and receive signals in all directions. While omnidirectional antennas theoretically allow for multiple signal paths from various directions, our analysis and experimental results demonstrate that the physical nature of corner scenarios inherently leads to two dominant paths. This is because other potential paths undergo multiple reflections, resulting in significant signal attenuation. Specifically, paths other than the reference path and the dominant human-reflected path experience additional reflections, leading to substantially weaker signal strength due to reflection losses. Therefore, despite the omnidirectional characteristics of the antennas, the corner geometry naturally emphasizes these two dominant paths while attenuating other potential multipath components.

Appendix 3: Verification of Linear Uncorrelation Between the Reference Path and Paths in Ω_2

To that end, we now go through a verification process to show that the component $w_r(f, t_n) = \cos(\phi_r(f, t_n) + \phi_a)$ associated with the reference path exhibits zero linear correlation with any component $w_i(f, t_n) = \cos(\phi_i(f, t_n) + \phi_a)$ associated with paths in $\Omega_2(t_n)$.

Consider that for any path i in $\Omega_2(t_n)$, its phase $\phi_i(f, t_n)$ can be decomposed into two terms given by

$$\phi_i(f, t_n) = \phi_i^{(r)}(f, t_n) + \phi_i^{(p)}(f, t_n) \quad (26)$$

where $\phi_i^{(r)}(f, t_n)$ represents the phase introduced by robot motion and reflection, and hardware impairments, and $\phi_i^{(p)}(f, t_n)$ denotes the phase introduced by human motion and reflection. While $\phi_i^{(r)}(f, t_n)$ varies among different paths, all $\phi_i^{(p)}(f, t_n)$ are independent of the phase of the reference path $\phi_r(f, t_n)$. We now define \mathbf{w}_r and \mathbf{w}_i as two sets of phase measurements sampled at time instances $t_n, n = 1, \dots, N$, given by

$$\mathbf{w}_r = \{\cos(\phi_r(f, t_n) + \phi_a)\}_{n=1}^N, \quad \mathbf{w}_i = \{\cos(\phi_i(f, t_n) + \phi_a)\}_{n=1}^N. \quad (27)$$

We then need to prove that for any arbitrary path i in $\Omega_2(t_n)$, the following condition holds

$$\rho_{\mathbf{w}_i, \mathbf{w}_r} \rightarrow 0, \quad \forall i \in \Omega_2(t_n), \quad (28)$$

where $\rho_{\mathbf{w}_r, \mathbf{w}_i}$ denotes the Pearson correlation coefficient between \mathbf{w}_r and \mathbf{w}_i , and \rightarrow denotes convergence to. Mathematically, $\rho_{\mathbf{w}_r, \mathbf{w}_i}$ is defined as:

$$\rho_{\mathbf{w}_r, \mathbf{w}_i} = \frac{\text{Cov}(\mathbf{w}_r, \mathbf{w}_i)}{\sigma_{\mathbf{w}_r} \sigma_{\mathbf{w}_i}}, \quad (29)$$

where the covariance is given by $\text{Cov}(\mathbf{w}_r, \mathbf{w}_i) = \mathbb{E}[\mathbf{w}_r \mathbf{w}_i] - \mathbb{E}[\mathbf{w}_r] \mathbb{E}[\mathbf{w}_i]$.

Recall that $\phi_r(f, t_n) = \frac{2\pi f}{c} l_r(t_n) + \sigma_r(t_n) + \vartheta(f, t_n)$. The phase variations induced by $l_r(t_n)$ and $\vartheta(f, t_n)$ result in $\phi_r(f, t_n)$ being approximately uniformly distributed over $[0, 2\pi]$. With sufficient samples, we have: $\mathbb{E}[\cos(\phi_r(f, t_n))] \rightarrow 0$ and $\mathbb{E}[\sin(\phi_r(f, t_n))] \rightarrow 0$. For the i -th path in $\Omega_2(t_n)$, where $\phi_i(f, t_n) = \phi_i^{(r)}(f, t_n) + \phi_i^{(p)}(f, t_n)$, similar properties hold: $\mathbb{E}[\cos(\phi_i(f, t_n))] \rightarrow 0$, $\mathbb{E}[\sin(\phi_i(f, t_n))] \rightarrow 0$, $\mathbb{E}[\cos(\phi_p(f, t_n))] \rightarrow 0$, and $\mathbb{E}[\sin(\phi_p(f, t_n))] \rightarrow 0$. Additionally, $\phi_i^{(r)}(f, t_n)$ and $\phi_i^{(p)}(f, t_n)$ are independent. With these conditions, we first have the following equations by applying the linearity property of the expectation operation:

$$\mathbb{E}[\mathbf{w}_r] = \mathbb{E}[\cos(\phi_r(f, t_n) + \phi_a)] \rightarrow 0, \quad \mathbb{E}[\mathbf{w}_i] = \mathbb{E}[\cos(\phi_i^{(r)}(f, t_n) + \phi_i^{(p)}(f, t_n) + \phi_a)] \rightarrow 0. \quad (30)$$

Given the independence of $\phi_r(f, t_n)$ and $\phi_i^{(p)}(f, t_n)$, we further have

$$\begin{aligned} \mathbb{E}[\mathbf{w}_r \mathbf{w}_i] &= \mathbb{E}[\cos(\phi_r(f, t_n) + \phi_a) \cos(\phi_i(f, t_n) + \phi_a)] \\ &= \mathbb{E}[\cos(\phi_r(f, t_n) + \phi_a) \cos(\phi_i^{(r)}(f, t_n) + \phi_i^{(p)}(f, t_n) + \phi_a)] \\ &= \mathbb{E}[\cos(\phi_r(f, t_n) + \phi_a) (\cos(\phi_i^{(r)}(f, t_n) + \phi_a) \cos(\phi_i^{(p)}(f, t_n)) - \sin(\phi_i^{(r)}(f, t_n) + \phi_a) \sin(\phi_i^{(p)}(f, t_n)))] \\ &= \mathbb{E}[\cos(\phi_r(f, t_n) + \phi_a) \cos(\phi_i^{(r)}(f, t_n) + \phi_a)] \cdot \mathbb{E}[\cos(\phi_i^{(p)}(f, t_n))] \\ &\quad - \mathbb{E}[\cos(\phi_r(f, t_n) + \phi_a) \sin(\phi_i^{(r)}(f, t_n) + \phi_a)] \cdot \mathbb{E}[\sin(\phi_i^{(p)}(f, t_n))] \\ &\rightarrow 0 \end{aligned} \quad (31)$$

Therefore, $\text{Cov}(\mathbf{w}_r, \mathbf{w}_i) \rightarrow 0$, and consequently $\rho_{\mathbf{w}_r, \mathbf{w}_i} \rightarrow 0$. We thus can conclude that the linear correlation between the reference path and any human-reflected path in $\Omega_2(t_n)$ approaches zero. According to **Property 2** (Appendix 1) of PCA, recall that \mathbf{w}_r represents the reference path component and \mathbf{w}_i represents the human-reflected path component, where these components are analogous to g and h discussed in **Property 2**. Since these paths exhibit negligible linear correlation ($\mathbb{E}[(\mathbf{w}_i - \mathbb{E}[\mathbf{w}_i])(\mathbf{w}_r - \mathbb{E}[\mathbf{w}_r])] \approx 0$), PCA separates them into distinct principal components, enabling effective isolation of the reference path component from human-reflected paths.

Appendix 4: CornerSense with Both Tx and Rx on the Robot

While CornerSense was primarily designed for scenarios where the AP (Tx) is fixed and only Rx is mobile, we demonstrate here that the system remains effective even when both Tx and Rx are mounted on the robot.

According to our theoretical framework, the scenario still maintains a reference path that solely contains the robot's movement and a dominant human-reflected path. Additionally, there exist paths with nearly constant lengths (blue and red dashed paths in 18①) that behave similarly to static paths. Due to their almost constant lengths, these paths exhibit minimal variance in their principal components (with nearly constant amplitude and phase variations only due to phase offsets), thus ranking lower in all principal components. Consequently, using our two-stage PCA extraction process, our system can still extract two dominant paths and remove robot motion effects and phase offsets. To verify this analysis, we conducted experiments with both Tx and Rx mounted on the robot, as shown in Figure 18②. We performed proximity detection for a target around a corner. Figure 18③ demonstrates that our metric exhibits the expected behavior: increasing when the target approaches the corner, decreasing when moving away, and remaining stable when no target is present. These results confirm that CornerSense maintains its effectiveness even when both the Tx and Rx are on the robot.

However, under certain device configurations and environmental conditions, the variance of phase offsets can become significant. In such cases, the blue and red dashed paths in Figure 18① may not consistently exhibit minimal variance in our two-stage PCA extraction process. This limitation necessitates alternative methods for identifying the two components associated with the reference path. One potential solution is to apply mutual information analysis. Specifically, while the reference path encodes both robot motion and phase offsets, the

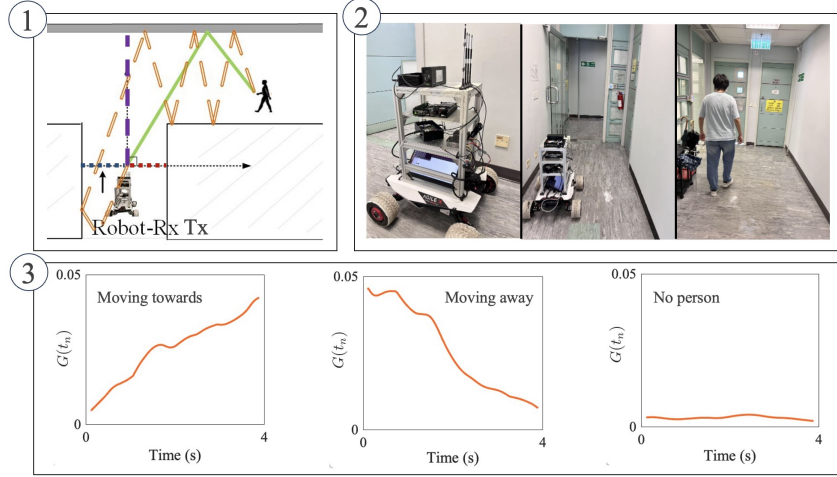


Fig. 17. Tx and Rx are both on the robot.

blue and red dashed paths primarily reflect phase offsets. By computing the mutual information between each principal component and the robot's motion, we can identify the relevant components, as those associated with the reference path will exhibit higher mutual information with the robot's motion. Although this issue did not arise in our current experimental setup, we present this basic idea as a potential direction for future research. The algorithmic implementation and experimental validation are left as future work.

Appendix 5: Target-Robot Distance Estimation

CornerSense can obtain the dominant human-reflected path after removing robot motion effects and calculate the distance between the target and the robot using two different methods.

The first method, as illustrated in Figure 18, involves a corner scenario with a fixed AP where the robot carries the Rx. After obtaining G from Equation 21, and knowing the AP position (and consequently the reference path length $l_r(t_0)$), we can derive $l_u''(t_n)$, which corresponds to the length of the green path in the Figure 18. Subsequently, we can calculate the distance between the target and the robot (represented by the bold blue line in the Figure 18) using the green path length along with known parameters: L_{Tx} (the distance from Tx to the corner), L_1, L_2 (corner dimensions), and the AoA θ_i . Given the geometric relationships shown in Figure 18, we first define the following notations where L_{xy} represents the length of line segment connecting points x and y as labeled in Figure 18(2). Using these notations, we can establish the following system of equations:

$$L_{ab} = L_1 - L_{fd}, \quad (32)$$

$$L_{bc} = \tan(\theta_i) * (L_1 - L_{fd}), \quad (33)$$

$$L_{cd} = L_{de} = \tan(\theta_i) * L_{fd}, \quad (34)$$

$$L_{ac} + L_{cf} + L_{fe} + L_{Tx} - (L_{bc} + L_{cd} + L_{de} - L_2) = l_u'', \quad (35)$$

where $\theta_i, L_1, L_2, L_{Tx}$, and l_u'' are known parameters. By solving this system of equations, we can determine all unknown variables. The distance between the target and robot can then be calculated as:

$$d_{target} = L_{ab} + L_{bc} + L_{cd} + L_{de}. \quad (36)$$

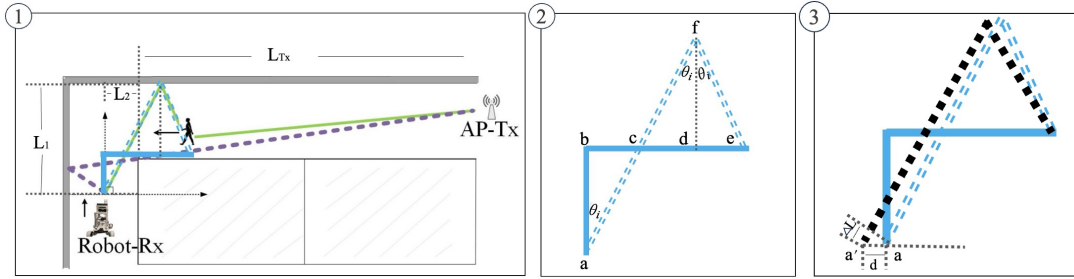


Fig. 18. The geometric model used for distance estimation between the target and robot.

After substitution and algebraic manipulation, this yields:

$$d_{target} = L_1(1 + \tan(\theta_i)) + \frac{\tan(\theta_i) - 1}{2 \tan(\theta_i)}(l_u'' - L_{Tx} + L_4). \quad (37)$$

The derived solution requires L_{Tx} as an input parameter, representing the path segment length from Tx to the corner edge as shown in Figure 18. However, this assumption of a horizontal path may introduce errors in practical scenarios where the actual path deviates from the horizontal plane. Our empirical evaluation across 10 datasets showed that the estimation error in target-to-robot distances fell within (0, 0.5) meters.

In our second method for estimating the target-to-robot distance, we consider placing both Tx and Rx on the robot. This configuration eliminates the need for Tx position information, thereby reducing potential errors in the final distance calculation. When both Tx and Rx are mounted on the robot, we only need to focus on the region marked as ② in Figure 18, where the obtained l_u'' equals the length of blue double-dashed line plus black bold dashed line. Specifically, we can establish the following geometric relationships:

$$L_{ab} = L_1 - L_{fd}, \quad (38)$$

$$L_{bc} = \tan(\theta_i) * (L_1 - L_{fd}), \quad (39)$$

$$L_{cd} = L_{de} = \tan(\theta_i) * L_{fd}, \quad (40)$$

$$2 * (L_{ac} + L_{cf} + L_{fe}) + \Delta L = l_u'', \quad (41)$$

where ΔL is the length difference between the black bold dashed line and blue double-dashed line. When the distance between the Tx and Rx antennas is d , we can obtain $\Delta L = d \sin(\theta_i)$. By solving this system of equations, we can determine all unknown variables. The distance between the target and robot can then be calculated as:

$$d_{target} = L_{ab} + L_{bc} + L_{cd} + L_{de} \quad (42)$$

After substitution and algebraic manipulation, this yields:

$$d_{target} = L_1(1 + \tan(\theta_i)) + \frac{\tan(\theta_i) - 1}{4 \tan(\theta_i)}l_u'' - \frac{\tan(\theta_i)}{2(1 - \tan(\theta_i))}\Delta L. \quad (43)$$

When Tx and Rx are mounted on the robot as shown in Figure 18③, even though they are not exactly co-located and have a small separation distance d (for example, Tx at point a and Rx at point a' in Figure 18③), we can accurately reconstruct the complete path length (sum of blue double-dashed line and black bold dashed line) using the measured AoA θ_i and the separation distance d . Therefore, unlike the first method where we need to know the distance from Tx to the corner edge (L_{Tx}), this approach avoids the significant errors that L_{Tx} would introduce in the first method. Our empirical validation across 10 datasets demonstrated that the absolute deviation

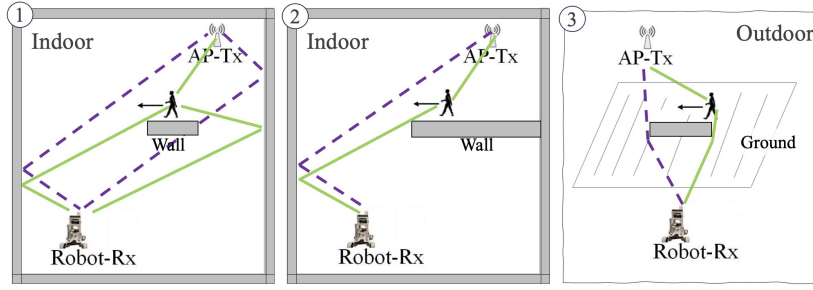


Fig. 19. Indoor NLoS and Outdoor Environments. The purple dashed lines represent the dynamic paths that only reflect off walls without human reflection, while the green solid lines indicate the dominant human-reflected paths.

between estimated and actual target-to-robot distances fell within (0, 0.3) meters, showing notable improvement in accuracy over the first method.

Appendix 6: Analysis of CornerSense's Applicability in Other Indoor NLoS and Outdoor Environments

This appendix examines the applicability and limitations of our approach in two different scenarios: indoor NLoS environments with complex wall structures and outdoor environments. We analyze how the characteristics of signal propagation and path composition in these environments affect our ability to extract and process the dominant human-reflected path.

As shown in Figure 19(1), we can observe a scenario where the target is located behind a small obstacle wall in an indoor environment. Due to the limited size of the obstacle, there exist multiple purple dashed dynamic paths with single reflection that only contain robot motion. Additionally, there are multiple green solid paths with two reflections that involve human reflection. Notably, the two green solid paths that traverse through the target exhibit high correlation, as they both contain robot and target motion components, and share nearly identical path segments from Tx to the target. This high correlation makes it difficult to separately extract these two green solid paths using PCA, preventing us from obtaining a pure dominant human-reflected path. In this case, although we can still obtain a strong reference path that only contains robot motion, which enables phase offset extraction and compensation from the raw CSI, we cannot accurately extract the dominant human-reflected path due to interference from other highly correlated path components.

However, indoor environments are not always this challenging. As illustrated in Figure 19(2), when the obstacle wall is normally connected to the surrounding walls - a more common scenario in residential settings - both the purple dashed reference path and the green solid dominant human-reflected path are distinctly presented as single paths. In this scenario, CornerSense can effectively extract both paths and proceed with robot motion and phase offset compensation for the dominant human-reflected path, ultimately obtaining accurate and pure target motion information.

After analyzing indoor scenarios, we further explore the performance of CornerSense in outdoor environments. As illustrated in Figure 19(3), in outdoor environments where obstacles such as trees or trash bins (represented by gray rectangles in the figure) are common, the path composition is relatively simpler. The figure shows one reference path that only contains robot motion with single attenuation loss, and one dominant human-reflected path that experiences two losses through both the target and the obstacle. The relative strength relationship between these two paths is also well-defined. After obtaining these two paths, we can apply our RMPOC algorithm to perform robot motion and phase offset compensation on the dominant human-reflected path, thereby extracting pure target motion information.